ChemPhysChem

Review
doi.org/10.1002/cphc.202200241

Chemistry Europe
European Chemical Societies Publishing

www.chemphyschem.org

Adducing Knowledge Capabilities of Instrumental Techniques Through the Exploration of Heterostructures' Modification Methods

Timothy M. Underwood[a] and Ross S. Robinson*[a]

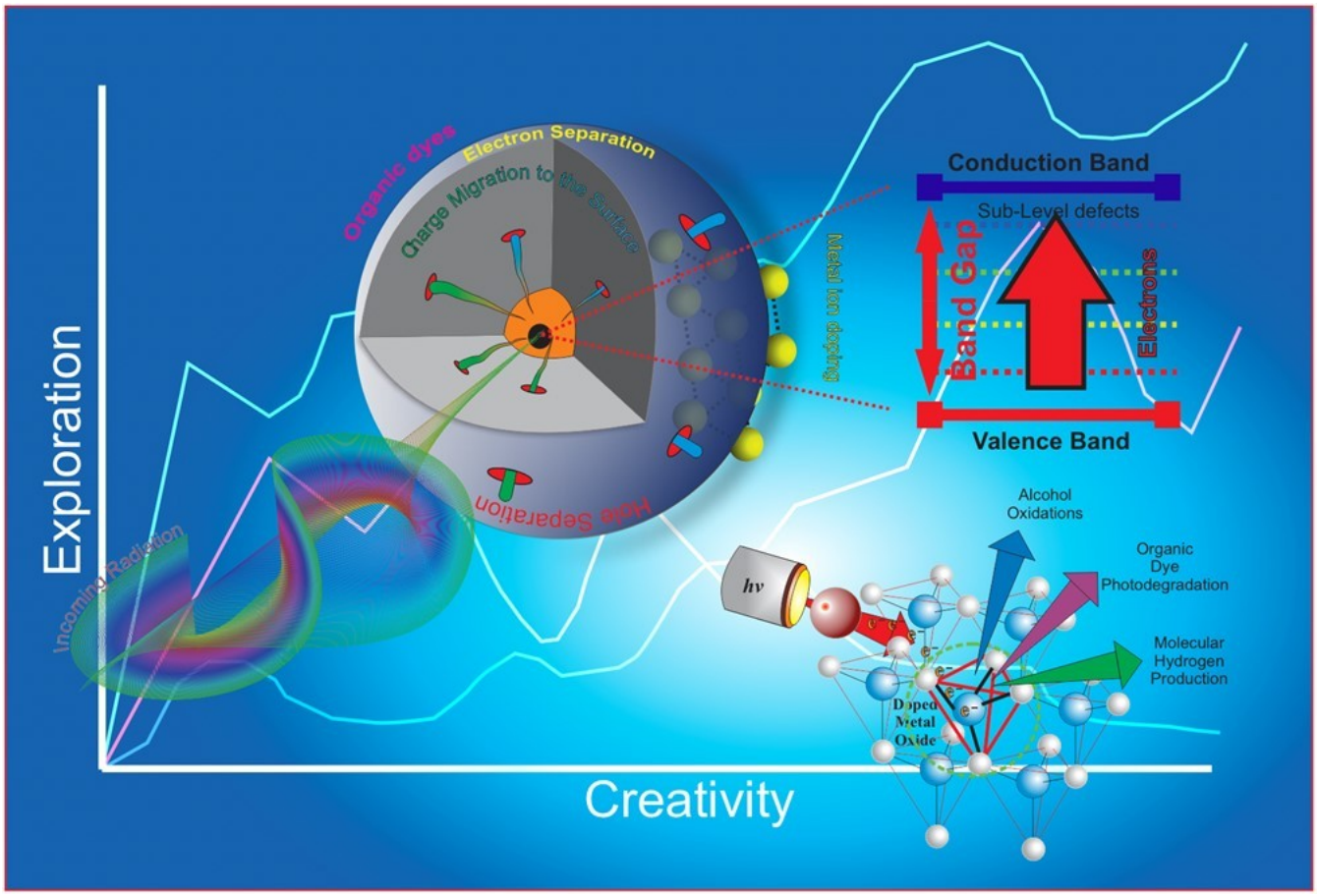

The ongoing evolution of technology has facilitated the global research community to rapidly escalate the constant development of novel advancements in science. At the forefront of such achievements in the field of photocatalysis is the utilisation, and in oftentimes, the adaptation of modern instrumentation to understand photo-physical properties of complex heterostructures. For example, coupling in-situ X-ray Raman scattering spectroscopy for real-time degradation of catalytic materials.

In this review, the capabilities of instrumental techniques and the opportunity to incorporate their functionality into potentially unforeseen applications is exemplified. Whilst discussing the importance of such instrumentation, the photo-physical mechanisms of various heterogeneous semiconductors have been included to demonstrate case-study examples for the suitability of various techniques, such as X-ray powder X-ray diffraction, microscopy (TEM and SEM), Raman spectroscopy, photoluminescence spectroscopy, computation models, and electron spin resonance spectroscopy to name a few.

1. Introduction

1.1. Research Overview

This review has aimed to observe the capabilities of modern instrumentation in an effort to allow the readership to consider unconventional uses of the said techniques and discovery unexpected knowledge. For example, whilst transmission electron microscopy (TEM) has demonstrated excellence in atomic resolution of both inorganic and organic materials; studying the electronic and magnetic properties, shape, size, crystal structure and chemistry of various materials, the microscope inherently suffers from high energy radiation that damages biological tissue. As a means to overcome this limitation, Trépout[1] investigated a sparse data collection model using an algorithmic data-missing modelling approach to limit radiation damage and offset the sparse data collection of resin-fixed and chemically-fixed embedded *Trypanosoma brucei* cells. Using 3D tomography of "thick" biological specimens using this new approach, Trépout[1] was able to reduce radiation damage of the analysed biological tissue.

The literature has reported an abundance of novel approaches to utilise instrumental techniques for advanced learning and scientific discoveries. Therefore, as a primary consideration to explain the enhancements in heterogeneous catalytic materials; their conversion, yield and selectivity results (a convincing measure to depict how invaluable various spectroscopic, microscopic and X-ray techniques are) are described. The presented research has utilised an array of photocatalytic materials to convey the proposed study presented herein below. Chapters 1 through 1.4 detail fundamentals of photocatalyst photochemistry, meanwhile Chapter 2 has focused on observing a concise review of the literature pertaining to organic dyestuff degradations.

Although, it is understood that the vast majority of analytical techniques, their capabilities and the numerous photocatalytic schemes, on which they can be applied, cannot be justifiably reported within one review. Therefore, the input to provide a concise summation of recent findings is presented through the lens of recent advances in heterogeneous catalysis.

1.2. Background Theory to Wide Band Gap Semiconductors

For semiconductors to operate effectively in a photocatalytic environment, an intensive knowledge of band gap energies, which underpins their success of photoactivation is required.

Large band gap energies greater than 2.0 eV (619.9 nm) categorise semiconductors as 'wide-band gap' photocatalysts that typically require irradiation sources at or below ultraviolet wavelengths ($\lambda < 400$ nm) for the necessary energy to photoactivate the semiconductor (Figure 1).

After supplying the required energy, an electron is promoted from the valence to conduction band, and an exciton pair is generated. The charges (a free electron and positive hole) migrate to the semiconductor's surface where redox processes occur.[2,3,4] The energy of a semiconductor's band gap (E) can be related to the respective wavelength (λ) through the following relationship (Equation 1):

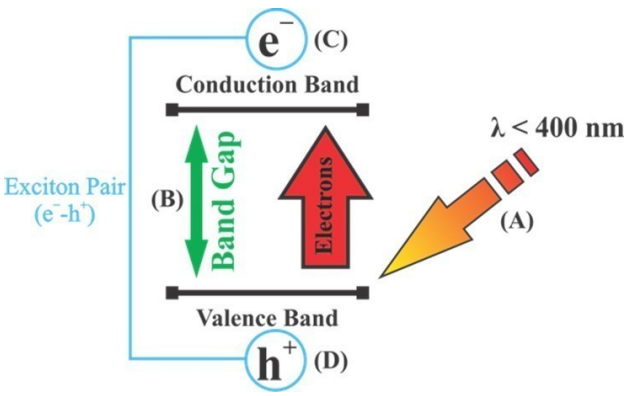

Figure 1. An illustration to represent the band gap excitation at specific energy inputs. When the incoming radiation (A) matches or exceeds the wide band gap energy (B), exciton pairs are generated. Thus electrons (C), and holes (D) migrate to the surface of the semiconductor.

[a] *Dr. T. M. Underwood, Prof. R. S. Robinson*
School of Chemistry and Physics,
University of KwaZulu-Natal
Private Bag X01, Scottsville, Pietermaritzburg, 3209, South Africa
E-mail: robinsonr@ukzn.ac.za

$$E = h\nu, \text{ where } \nu = \frac{c}{\lambda}, \quad E = \frac{hc}{\lambda} \tag{1}$$

The band gap energy (E) of semiconductors is commonly reported in units of electron volts (eV), therefore; for wavelength (λ) in nm (Equation 2),

$$E\ (\mathrm{eV}) = \frac{1240\ \mathrm{eV\ nm}}{\lambda}, \tag{2}$$

where the coefficient, **1240** has been calculated from $\frac{hc}{10^{-9}\,e}$ and $\mathbf{1\,nm = 10^{-9}\,m}$.

In the above expressions, h is the (Planks Constant $= 6.626 \times 10^{-34}$ Js), c (speed of light in free space $= 2.998 \times 10^{8}$ ms^{-1}), and e (electron's elementary charge $= 1.602 \times 10^{-19}$ C).

In this review's scope and within the context of discussing heterogenous photocatalysis, an array of metal oxide materials have been examined. Amongst which include representative examples; thiophene-based covalent triazine frameworks, amorphous Ni-$Mn_{0.3}Cd_{0.7}S$ with sulfur vacancies, Ti_3C_2Tx and ultrathin N-$ZnIn_2S_4$, anatase TiO_2 doped with caron black, spray-dried g-C_3N_4/TiO_2 nanocomposite granules, zinc- and titanium-layered double hydroxides, Pt–Pd/Ta_2O_5, Ag–ZnO–CdO, CdS/TiO_2, SnO_2–ZnO–$ZnWO_4$, metal organic framework photo-catalysts MIL-125/Ag/g-C_3N_4,α-Fe_2O_3/Cu_2O, g-C_3N_4/Bi_2MoO_6. The discussion of such metal oxide system have been identified to exemplify the broad scope of current methodologies to develop photo-active compounds, how they operate and coupled to their respective developments in the field of heterogeneous photocatalysis.[2]

As depicted in Figure 2, the respective valence and conduction bands of numerous photocatalysts have been listed. The significance of such information has allowed scientists to capitalise on the various potentials (V), for strategising numerous approaches to develop (non)metal doping strategies, heterojunctions and dye surface loadings for photo-redox transformations of both organic and inorganic species.

The value in identifying the positioning of the valence bands (bottom grey rectangles) and conduction bands (upper grey rectangles) of Figure 2 is important to develop a photocatalyst for the intended purpose. For example, SnO_2 has the potential for the oxidative splitting of water at H_2O/O_2 (0.82 V), yet the conduction band is lower than $2H^+/H_2$ (−0.41 V), therefore impractical for hydrogen reduction projects. Despite SnO_2 not intrinsically having the potential for H_2 evolution, the possibility exists to either couple, dope or surface modify the surface of the chosen metal oxide for extending the applications beyond its intrinsic limitations as described in Chapter 1.3. Modes of Functionalising Semiconductors.

1.3. Modes of Functionalising Semiconductors

An important consideration when studying 'doped' heterogeneous catalysts is the nature of how extrinsic species are incorporated into or on the semiconductor's lattice. Most dopant-incorporation studies into a semiconductor are beyond the scope of this review (the current research will only reflect on the instrumental insight into the interpretation of heterogeneous semiconductors). However, the text below shall highlight their theory.

The term 'doping' of semiconductors has been commonly used in the literature' to describe techniques where metal oxides are modified (through ion-exchange) or addition of foreign atoms to enhance the oxidative and reductive capabilities. Precursors to the metal oxides and their future dopants are utilised in various methodologies such as, hydrothermal, sol-gel, microemulsion, gas condensation, co-precipitation, microwave assisted, ion spluttering, template synthesis and ion spluttering approaches to develop modified heterogeneous catalysts (Scheme 1).

Doping a semiconductor can proceed *via* four various routes (Scheme 1); namely, ion implantation into the semiconductor's lattice through metal and or non-metal ion exchange (substitution), interstitial ion incorporation, surface adhesion (of either metal, non-metal or organic linker particles) and lastly semiconductor-semiconductor heterojunctions. Methods of doping the surface of semiconductors using metals, non-metals and organic linkers do not directly affect the lattice, however the extrinsic inclusion of a foreign material onto the heterogeneous catalyst's surface warrants its discussion and elaboration in the proceeding texts.

Professor Ross Robinson completed his PhD at Rhodes University and is currently a Professor of Organic Chemistry at the University of KwaZulu-Natal and the current Dean and Head of the School of Chemistry and Physics. His research interests lie in organic synthesis, photocatalysis and materials science.

Dr. Timothy Underwood completed his undergraduate degree in Chemistry and Chemical Technology at the University of KwaZulu-Natal, South Africa (2011). Subsequently, he was under the supervision of Professor Ross Robinson from Honours (2012) with an attentive focus of semiconductor mediated photocatalysis and solid-state metal oxides until obtaining his doctorate in 2019.

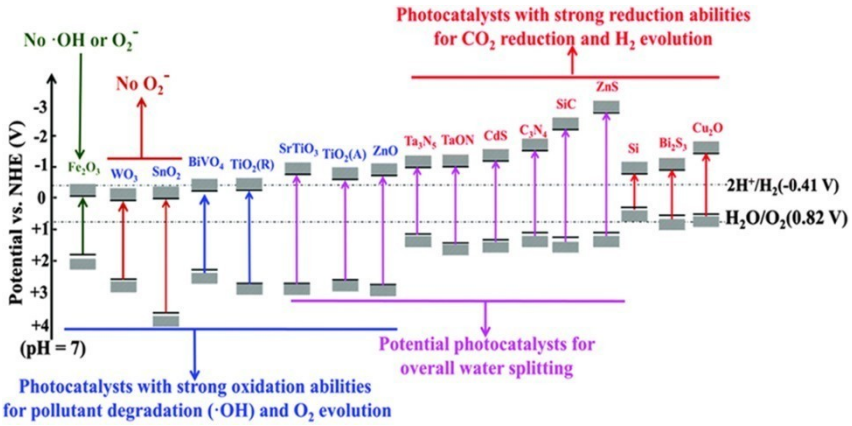

Figure 2. Band gaps of common photocatalysts, including the respective valence and conduction bands vs. NHE (V). Adapted with permission from Ref. [3] Copyright (2018) Elsevier.

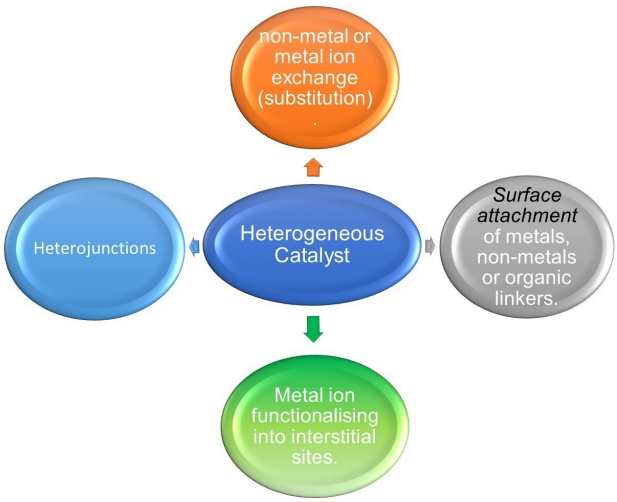

Scheme 1. The three modes of functionalising heterogeneous semiconductors.[4,5]

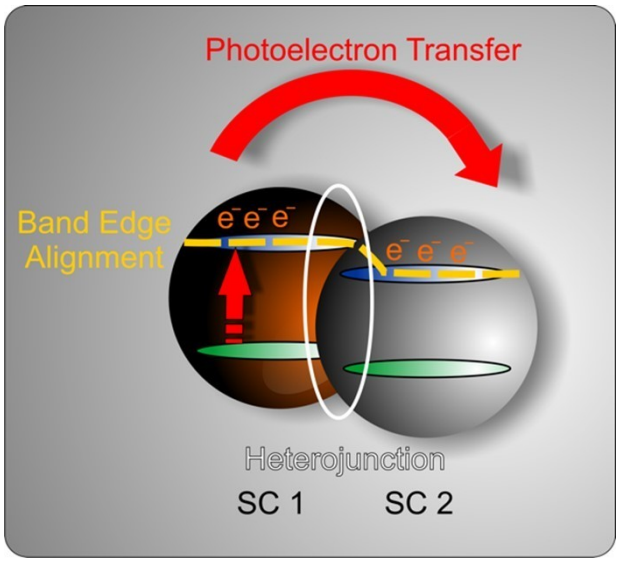

Figure 3. Sketched illustration depicting the exemplary CdS/TiO_2 (SC 1/SC 2) heterojunction between SC 1 and SC 2, with photoelectron ejection from the higher energy conduction band of CdS and into the lower energy conduction band of TiO_2.

1.4. Photocatalytic Reports of Semiconductor Heterojunctions

1.4.1. Straddling, Staggered, and Broken Heterojunction Band Gaps

As described in the literature, an interface which forms between two different band structures of two dissimilar semiconductors that can lead to the alignment of the band structure pair, is known as a 'heterojunction'.[6]

Heterojunction research between two semiconductors continues to expand with novel methods to synthesise, characterise and understand the light absorptivity, photo excitations (excitons) and physical mechanics of the solid-state materials. Instrumental methodologies that have evaluated the three aspects of photonics; correct heterojunction pairing, band edge alignments, and photoelectron transfers (Figure 3) between semiconductors are discussed.

As previously shown in Scheme 1 (viz metal or non-metal ion exchange [substitution], metal ion doping into interstitial sites, or surface loading of metals, non-metals or organic dyes), the methods to functionalise semiconductors are much akin the technique of forming a heterojunction between two semiconductors. The objective of the heterojunction utilises the redox positions of two dissimilar semiconductors to optimise band edge alignment for an array of synthetic-organic transformations under visible light conditions.[7–9,2l]

A well-known heterojunction exists between cadmium sulfide and titanium dioxide (CdS/TiO_2).[2h,i] The efficiency of CdS/TiO_2 to transfer photoelectrons from the visible-light-activated cadmium sulfide (2.4 eV, 517 nm) to ultraviolet-light-activated titanium dioxide (3.2 eV, 387 nm^4) is accomplished through close contact of the CdS/TiO_2 heterojunction.

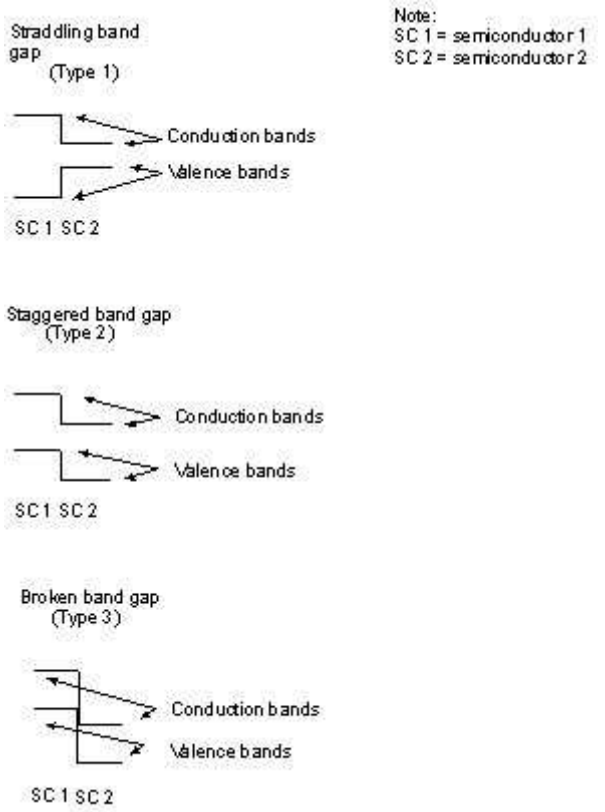

Figure 4. The three possible band gap schemes for valence and conduction band pairs of two heterojunctioned semiconductors: straddling (Type 1), staggered (Type 2), and broken (Type 3).

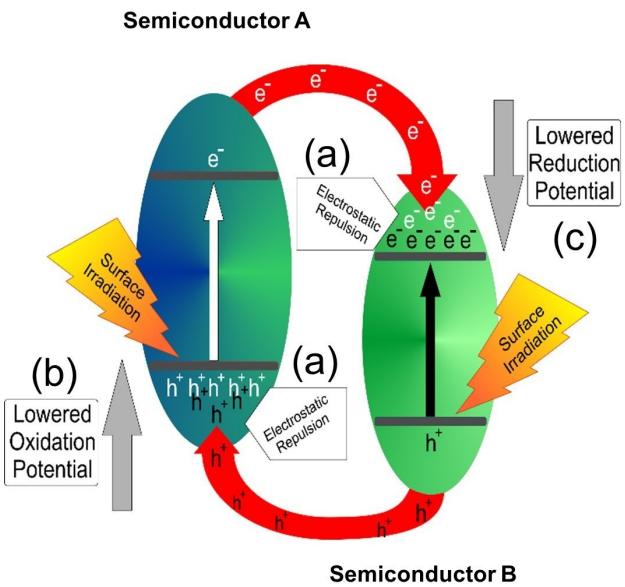

Figure 5. Inherent limitations of heterojunctions (Type 1, 2 and 3). Electrostatic repulsion from the accumulation of either e^- and/or h^+ in separate band states (a), and lowered oxidation and reduction potentials (b and c, respectively).

Literature has reported five photoelectron migration mechanisms that occur between two semiconductors. The first three are described in Figure 4.

According to literature,[10] one of five potential heterojunction systems can exist between two different (p- and n-Type) semiconductors, namely, straddled (Type 1), staggered (Type 2) and broken (Type 3) (Figure 4). Type 2 systems have been well reported in the chemical domain.[11] However, two significant drawbacks arise from conventional heterojunctions (Types 1, 2, and 3). Firstly, due to the electron migration from the higher conduction band of semiconductor A to the lower conduction band of semiconductor B, the redox potential of the conduction band electron is significantly reduced. The same conditions apply to the reduced oxidation potential of semiconductor B, after hole migration from semiconductor A. Furthermore, due to the influx of photoelectron migration from the conduction band of semiconductor A and into the conduction band of semiconductor B (of which is already electron rich), electrostatic repulsion forces arise (Figure 5).

However, more recently, additional heterojunction strategies have been identified, namely the fourth and fifth heterojunction systems known as the ***z-scheme*** and ***s-scheme***, which have received considerable attention due to their superior photoelectronic properties to minimise exciton recombination and inhibit weak photo-redox positive hole and photoelectron production. A brief elaboration on *Z*-schemes (originating from 2013) and more extensively S-scheme mechanisms has been discussed later in **Chapter 2.3.2**, *vide infra.*

Since the advent of semiconductor-mediated photocatalysis, a movement toward environmentally friendly catalysis to produce feedstock material is rapidly developing. Binary and tertiary photocatalytic systems are of particular interest amongst synthetic chemists.

Hamrouni and co-workers[2j] explored the possibility of attenuating the properties of zinc oxide after constructing a ternary SnO_2–ZnO–$ZnWO_4$ system (composed of two Type-II staggered heterojunctions constructed from ZnO|SnO_2 and ZnO|$ZnWO_4$) was discovered through a facile sol-gel technique to enhance the charge separation effect of ZnO and the impact on benzylic alcohol oxidation studies. 4-Methoxybenzyl alcohol was oxidised in the presence of zinc oxide with various tin and tungsten dopings. The authors provided a synopsis of the binary and tertiary systems and reported a 100% improvement in 4-methoxybenzyl alcohol conversion with a 10% increase in selectivity compared to zinc oxide alone. The experiments were conducted at 365 nm wavelength. Various instrumental techniques were utilised to identify why the ternary (SnO_2–ZnO–$ZnWO_4$) system had an apparent heightened visible light response through photoluminescence spectroscopy, powder X-ray diffraction and powder UV/Vis spectroscopic studies.

Photoluminescence spectroscopy identified that all three complex ternary derivatives of SnO_2–ZnO–$ZnWO_4$ depicted lower peak intensities (at red-shifted values greater than 450 nm, Figure 6, Spectra b, c, and d) than ZnO (Figure 6, Spectrum a) and were reported to originate from a reduction in radiative recombination of photogenerated electrons, and holes on the surface of zinc oxide. However, in order to optimise and

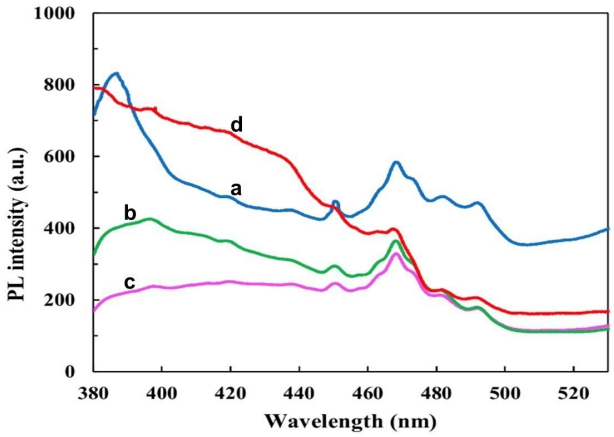

Figure 6. Photoluminescence spectra of intrinsic ZnO (blue, spectrum a), Zn–$ZW_{0.05}$ (green, spectrum b), Zn–$Sn_{0.05}$ (pink, spectrum c) and $Sn_{0.025}$–Zn–$ZW_{0.025}$ (red, spectrum d). The lowered peak intensities of the ZnO complexes (Spectra b, c, and d at $\lambda > 450$ nm) originated from reduced radiative recombinations compared to intrinsic ZnO. Adapted with permission from Ref. [2j] Copyright (2015) Elsevier.

thereby reduce exciton recombinations near the band gap of zinc oxide (380–440 nm), the SnO_2–ZnO–WO_4 ratios needed careful consideration as $Sn_{0.025}$–Zn–$ZW_{0.025}$, (Figure 6, Spectrum d) demonstrated poor band-edge exciton quenching characteristics compared to ZnO (Figure 6, Spectrum a).

Powder X-ray diffractograms identified the major crystalline phases in the compound SnO_2–ZnO–$ZnWO_4$ system as tetragonal SnO_2 (JCPDS card number: 41-1445), monoclinic $ZnWO_4$ (JCPDS card number: 15-0774), and hexagonal ZnO (JCPDS card number: 36-1451). However, after collecting complementary powder UV/Vis diffuse reflectance spectra (Figure 7), the Zn–$Sn_{0.05}$ (spectrum d), Zn–$ZW_{0.05}$ (Spectrum e) and $Sn_{0.025}$–Zn–$ZW_{0.025}$ (spectrum f) species produced poor absorbance characteristics compared to ZnO (spectrum a) and SnO_2 (spectrum b), which were suspected to arise from poor crystallinity of the ternary SnO_2–ZnO–$ZnWO_4$ systems. Furthermore, the undoped ZnO (Figure 7, spectrum a) and SnO_2 (Figure 7, spectrum b) were observed to retain higher optical absorbance values and lower cut-off wavelengths compared to the functionalised species. The spectra cut-off wavelength variations showed that doping ZnO and SnO_2 red-shifted the optical band gap and hence, improved visible light activities were detected.

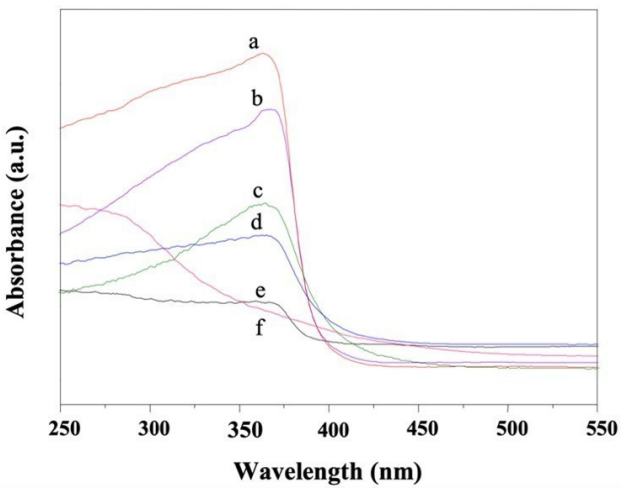

Figure 7. Powder UV/Vis diffuse reflectance spectra from the SnO_2–ZnO–$ZnWO_4$ mixed metal oxides. Spectra 'a' and 'b' represent ZnO and SnO_2, while spectra 'c' and 'd' depict $ZnWO_4$, Zn–$Sn_{0.05}$, Zn–$ZW_{0.05}$ and $Sn_{0.025}$-Zn–$ZW_{0.025}$, respectively. Adapted with permission from Ref. [2j] Copyright (2015) Elsevier.

This observation was subsequently corroborated by using scanning and transmission electron microscopy to identify nanoparticles of 20–150 nm in size. Compiling both photoluminescence, spectroscopic and microscopic data collected by Hamrouni and co-workers,[2j] they proposed a band analysis structure (Figure 8).

Two heterojunctions created through xerogels (ZnO|SnO_2 and ZnO|$ZnWO_4$), which when combined through a direct addition of $Zn(OAC)_2$, $SnCl_4$ and phosphotungstic acid hydrate (PTA) formed a dual-Type II heterojunction arrangement as depicted in Figure 8. The authors stipulated that a ZnO|SnO_2 and ZnO|$ZnWO_4$ arrangement was likely over a SnO_2|$ZnWO_4$ arrangement since the sample mainly consisted of ZnO.[2j] As observed in Figure 8, both heterojunctions would noticeable suffer from reduced redox potentials as electrons were transferred from the strong reductive conduction band of ZnO into SnO_2 and $ZnWO_4$, meanwhile positive hole migration from the stronger oxidative valence bands of SnO_2 and $ZnWO_4$ to ZnO, respectively. This unforeseen limitation in Type-II staggered

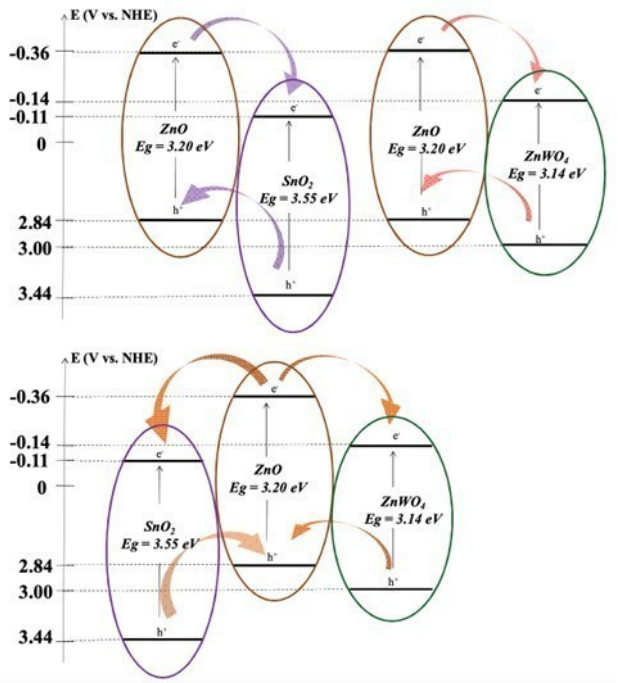

Figure 8. Band gap analysis structure as proposed by Hamrouni and co-workers, demonstrating the coupling between three metal oxides for the development of a tertiary system SnO_2-ZnO-$ZnWO_4$. Adapted with permission from Ref. [2j] Copyright (2015) Elsevier.

band alignment (lower photoredox potentials) have led to the ongoing development of Z- and S-scheme heterojunctions (*vide infra*).

In similar texts that also investigated complex semiconductors for oxidising organic substrates, Yang *et al.*,[2k] published a dual redox functioning silver nanoparticle mediated metal-organic framework (MOF) photocatalyst, 'MIL-125/Ag/C_3N_4' compound semiconductor (MIL-125 = $Ti_8O_8[O_2C{-}C_6H_5{-}CO_2]_6$) that operated as both an oxidant of alcohols to aldehydes and reductant of nitrobenzene to aniline in alcoholic solvents.

An interesting observation regarding the adhesion of silver nanoparticles to MIL-125 and graphitic carbon nitride (g-C_3N_4) semiconductors was reported. X-ray diffraction data revealed that (111) silver nanoparticles were unable to adsorb and form a Schottky surface on the MIL-125. However, after incorporating g-C_3N_4 with MIL-125, silver adhered to the surface of MIL-125 in the multicomponent semiconductor system. The authors[2k] never postulated why silver was only adsorbed in the presence of g-C_3N_4 which posed an interesting question to resolve. There was evidence reported in their FT-IR findings for g-C_3N_4 that revealed the presence of C–N heterocycles. This suggests possible Ag–N coordination and hence postulates the adhesion of MIL-125/Ag/g-C_3N_4 and not MIL-125/Ag. Further omitted evidence in the authors'[2k] X-ray photoelectron spectroscopic data were amino groups at 401.3 eV that substantiated the possibility of free nitrogen coordination sites.

Besides studying exciton lifetimes with photoluminescence spectroscopy and powder UV/Vis spectroscopy, Yang *et al.*[2k] explored the fast interfacial charge transfer dynamics of MIL-125/Ag/g-C_3N_4 using a three-component electrodic system using an AC impedance-potential model (saturated calomel reference electrode, platinum foil counter electrode and MIL-125/Ag/g-C_3N_4 as the working electrode). The electrode's reaction rate of a given study can be monitored from the arc radius of the electrochemical impedance Nyquist plot (Figure 9). A decrease in the arc radius indicates a fast-interfacial charge transfer and separation of the photogenerated exciton pairs occurring on the semiconductor's surface.[2k]

The application of electrochemical impedance spectroscopy characterised the positive photocatalytic effect arising from silver in the case of MIL-125/Ag/C_3N_4. Silver was incorporated into the MIL-125/C_3N_4 matrix to enhance the interfacial charge transfer between MIL-125 and C_3N_4 through the action of a bridging electron transfer agent (Ag).

Yang *et al.*[12] have also demonstrated the potential of electrochemical impedance spectroscopy to access the photoreactivity of complex semiconductors after studying a MIL-53(Fe) metal-organic framework (consisting of continuous $FeO_4[OH]_2$ units) doped with graphene (Figure 10). In the presence of graphene doping (Figure 10), the electrochemical impedance data demonstrated an improved exciton lifetime extension through electron migration across the MIL-53(Fe)-GR heterojunction.

While semiconductor heterojunctions have been utilised to exemplify excellent platforms for fine chemical synthesis, numerous studies have also been directed towards the remediation of dyes from wastewater streams and the decomposition of volatile organics *vide infra*, as graphically summarised in Figure 11.

In an organic dyestuff degradation of Rhodamine B published by Fagan *et al.*,[13] an attempt to elucidate the doping mechanics of g-C_3N_4 onto TiO_2 was investigated. After studying g-C_3N_4/TiO_2 using Fourier Transform Infrared spectroscopy (FTIR), they identified the major stretching (2900–3600 cm^{-1} as terminal NH_2/NH) and breathing (807 cm^{-1}) modes of g-C_3N_4. However, in g-C_3N_4/TiO_2, the authors could neither qualitatively confirm surface loading nor doping of g-C_3N_4 into TiO_2 (Figure 12). FTIR spectroscopy has further demonstrated applications elsewhere for phase compositions in WO_3/$CdWO_4$ materials for methylene blue, methyl orange, and rhodamine B degradation.[7]

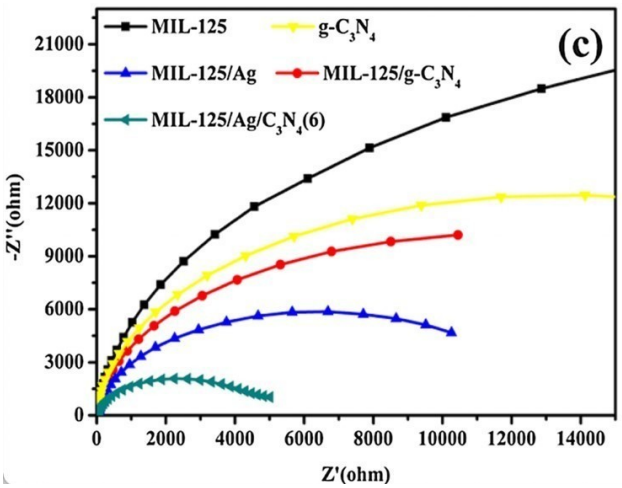

Figure 9. The observed arc radii for the electrochemical impedance of the investigated semiconductors (MIL-125, g-C_3N_4, MIL-125/Ag, MIL-125/g-C_3N_4, and MIL-125/Ag/C_3N_4), demonstrating the superior photo-efficiency of the MIL-125/Ag/C_3N_4 material. Adapted with permission from Ref. [2k] Copyright (2017) Elsevier.

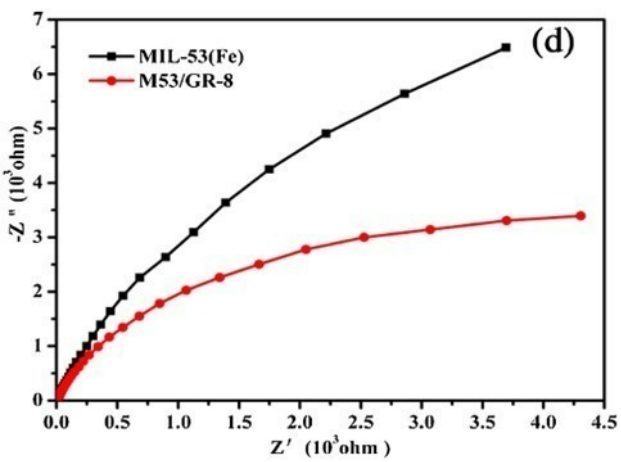

Figure 10. Nyquist plot of fast charge separation from MIL-53(Fe)/graphene (M53/Gr-8) opposed to MIL-53(Fe) alone. Adapted with permission from Ref.[12] Copyright (2016) Elsevier.

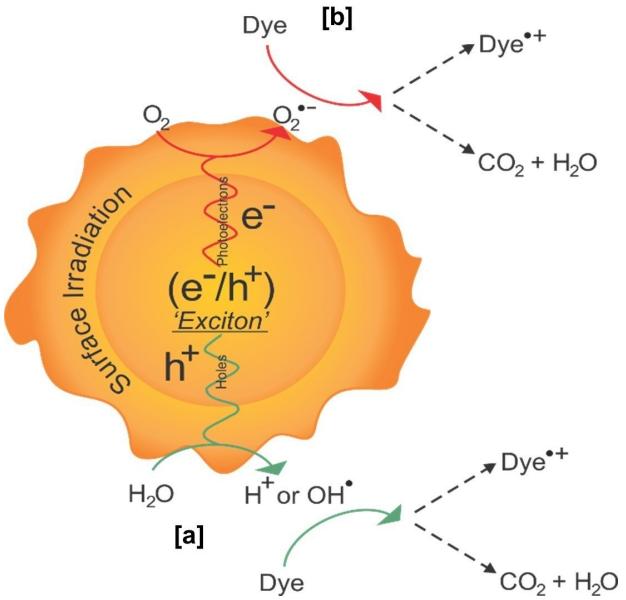

Figure 11. An illustration summarising the two possible visible-light driven photocatalytic pathways (hydroxyl [a] and superoxide [b] radicals) of semiconductors for dyestuff remediation studies.

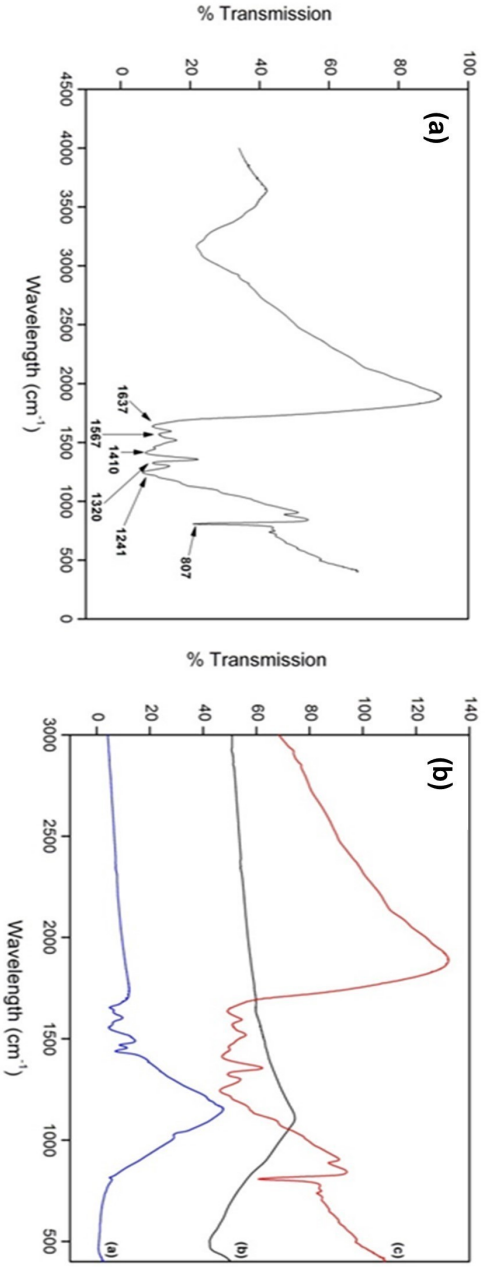

Figure 12. FTIR studies of g-C_3N_4 (a) and g-C_3N_4/TiO_2 (b) revealing the co-doping effect of coupling g-C_3N_4 and TiO_2. Note on g-C_3N_4/TiO_2 (right): a = 4 % g-C_3N_4-TiO_2, b = undoped TiO_2 and c = g-C_3N_4. Adapted with permission from Ref.[13] Copyright (2016) MDPI AG.

1.4.2. Z- and S-Scheme Heterojunctions in Photocatalysis

Various articles discussed in the literature have detailed the coupling of metal oxides for molecular oxygen reduction to hydrogen peroxide (H_2O_2) and lead oxidation (Pb^{2+} to PbO), gas sensoring and volatile organic compound remediation. However, their limitations in previous band structure modifications have lessened their potentials in photocatalysis[14–16] Therefore, it is important to emphasise the significance of the subsequent heterojunctions, the *Z*- and S-schemes. Whilst the Z-scheme heterojunction has demonstrated significant advances over the Type-II band alignment, limitations such as weakened redox pairs and repulsive charges between coupled valence bands (holes) and conduction bands (electrons) exist.[17] Therefore, a brief description of the Z-scheme has been provided below, upon which a discussion of the "Step" S-scheme heterojunction shall be discussed.

The first noted study of a hybrid all-solid *Z*-scheme couple (using g-C_3N_4 and TiO_2 [g-C_3N_4|TiO_2] heterojunction) *without* an electron mediator has been reported by Yu *et al.*[18] in 2013 on the photo-decomposition of gaseous formaldehyde. Similar *Z*-scheme research has been subsequently published on the reduction of carbon dioxide to methanol over Si/TiO_2,[19] formaldehyde decomposition on platinum ceramics,[20] hydrogen gas evolution over NiS/C_3N_4/CNT nanoparticles,[21] enrofloxacin photo-decomposition with carbon dot decorated TiO_2/C_3N_4 and the selective detection of Cu^{2+} while using a direct *Z*-scheme BiOI-CdS semiconductor.[22,23]

The '***direct Z-scheme mechanism***' affords a significantly improved mechanism over conventional heterojunctions (Figure 4) because a highly oxidative positive hole is retained on semiconductor **A**, meanwhile, photoelectron ejection into the electrostatically attracted valence band of semiconductor **B** enhances strongly reductive electron production (Figure 13).

Literature has also reported that *Z*-scheme heterojunctions with a staggered (Type 2) heterostructure are an effective photocatalytic means for hydrogen production from the semiconductors' heterojunction formation.[24,25]

Wang and co-workers[21] attempted to photocatalytically reduce carbon dioxide after constructing a direct *Z*-scheme heterojunction from Fe_2O_3 and Cu_2O (α-Fe_2O_3/Cu_2O). X-ray diffraction data verified that α-Fe_2O_3/Cu_2O consisted of cubic

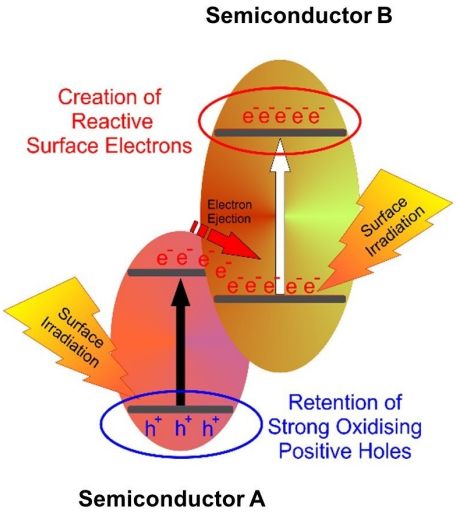

Figure 13. Exemplified exciton migration across the Z-scheme heterojunction. The positive hole (blue h+) remains in semiconductor A, meanwhile photogenerated electrons (red e⁻) are injected into the valence band of semiconductor B.

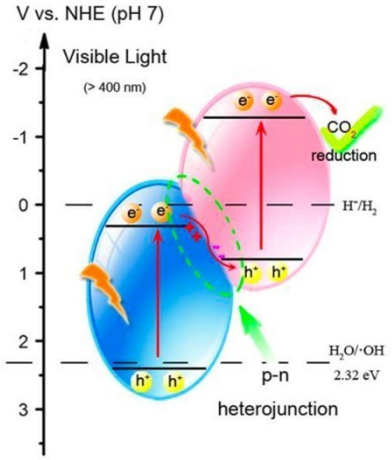

Figure 14. A schematic of the heterojunction formed between the band edge positions of Fe_2O_3 and Cu_2O. The 'heterojunctioned zone' (dashed green sphere) demonstrates the ejection of electrons from the conduction band of Fe_2O_3 and into the valence band of Cu_2O for CO_2 reduction. Adapted with permission from Ref. [2l] Copyright (2015) American Chemical Society.

Cu_2O (Powder Diffraction File™ [PDF] No: 01-078-2076), α-hematite (Fe_2O_3, PDF No: 01-086-2368) and no amalgam of Fe_2O_3 and Cu_2O was detected. Fast-Fourier transform (FFT) diffraction patterns did, however, reveal that Fe_2O_3 and Cu_2O were fused at the interface of both oxides. The enhanced photocatalytic activity arose from the α-Fe_2O_3/Cu_2O heterojunction, which ensured a high reduction potential. After irradiating for three hours using a 300 W xenon arc source, an optimal 50 mol% Cu_2O-Fe_2O_3 (50Cu–Fe) nanocomposite could produce 5 μmol g_{cat}^{-1} $CO_{(g)}$ at an H_2O/CO_2 ratio of 0.025 at 313 K.

During their study, the authors postulated an additional mechanism for carbon dioxide photo-reduction. This was later confirmed after deducing the relative valence and conduction band positions in the Cu_2O–Fe_2O_3 heterojunction. A method to determine band position and hence a possible means to evaluate the carbon dioxide photo-reduction was proposed from ultraviolet photoelectron spectroscopic measurements recorded on a Perkin Elmer PHI 5300 X-ray photoelectron spectrometer equipped with a HeI (21.2 eV) monochromatic light source. Wang and co-workers[2l] interpreted the ultraviolet photoelectron data using a linear intersection method (which estimated band edge positioning) and determined the valence band of Cu_2O to reside at −5.32 eV (*vs* vacuum) and a calculated Fermi level at −5.17 eV (*vs* vacuum).

Furthermore, with a knowledge of the relationship (Equation 1):

$$E_{abs} = E^{\theta} - 4.44, \text{ where : } E_{abs} = \text{vacuum energy}$$
$$E^{\theta} = \text{normal electrode potential}$$

The corresponding valence and conduction band positions could be determined (for Cu_2O, valence band [0.88 eV] and conduction band [−1.17 eV] *vs* normal hydrogen electrode) (Figure 14).

Previously reported in by Miyauchi *et al.*,[26] a *Z*-scheme photocatalytic system ($CaFe_2O_4/WO_3$) was prepared for the photocatalytic decomposition of acetaldehyde to carbon dioxide. Two methods (hydrothermal and mechanical mixing) were utilised to obtain 10% ($CaFe_2O_4/WO_3$). The hydrothermally prepared $CaFe_2O_4/WO_3$ (H) exhibited a superior carbon dioxide yield compared to the mechanically mixed ($CaFe_2O_4/WO_3$) (M).

The improved photocatalytic activity arising from $CaFe_2O_4/WO_3$ (H) was unknown at the time because the instrumental analysis using Brunauer-Emmett-Teller (B.E.T.) surface area measurements, powder X-ray diffraction (XRD) and ultraviolet-visible light spectrophotometry (UV-Vis) yielded identical physical characterisation between $CaFe_2O_4/WO_3$(H) and $CaFe_2O_4/WO_3$ (M).

Calculated BET measurements for $CaFe_2O_4/WO_3$ (H) and $CaFe_2O_4/WO_3$ (M) determined both species to have similar surface areas (12.9 m^2/g and 14.8 m^2/g respectively), thus concluding surface morphology was not the cause of $CaFe_2O_4/WO_3$ (H) having enhanced photocatalytic activity. The powder X-ray diffraction results depicted identical single phased and well-crystallised $CaFe_2O_4$ peaks with monoclinic WO_3 in both samples. Neither $CaFe_2O_4/WO_3$ (H) nor $CaFe_2O_4/WO_3$ (W) exhibited any peak shifting in the powder X-ray diffraction results, thus indicating no solid-state formation between $CaFe_2O_4$ and WO_3 in either sample. In addition, both $CaFe_2O_4/WO_3$ (H) and $CaFe_2O_4/WO_3$ (W) presented identical broad UV-Vis absorption profiles. However, scanning electron microscopy (SEM) results indicated that the $CaFe_2O_4/WO_3$ (H) preparation method yielded equally dispersed WO_3 particles in high concentrations on $CaFe_2O_4$. Meanwhile, WO_3 had aggregated significantly on the surface of $CaFe_2O_4/WO_3$ (W).

An important parameter to consider when synthesising heterostructured semiconductors is the zeta (ζ) potential. Zeta potentials measure electrostatic attraction/repulsion forces existing between particles within close proximity. Mis-matched

electrostatic charges affect solid stability and hence photocatalytic activity. Miyauchi *et al.*,[26] reported that zeta potential measurements for an isoelectric point of $CaFe_2O_4$ occurred at a *ca.* pH of 1.5. However, at this pH, WO_3 was reported to remain as a homogeneous colloidal suspension.

Therefore, Miyauchi *et al.*,[26] adjusted the pH to approximately neutral conditions, which promoted a negative $CaFe_2O_4$ surface charge and therefore encouraged the electrostatic attraction of W^{6+} cations. This lends reason to support the enhanced photocatalytic activity of $CaFe_2O_4/WO_3$ (H) over $CaFe_2O_4/WO_3$ (W), which arose from the electrostatically bound heterojunction of $CaFe_2O_4/WO_3$ (H) compared to the mechanically fixed $CaFe_2O_4/WO_3$ (W) composite. The electrostatically synthesised heterojunction of $CaFe_2O_4/WO_3$ (H) was identified to favour charge separation across the *Z*-scheme heterostructure.

The limitations of the Z-scheme highlighted by Miyauchi *et al.*,[26] and Mishra *et al.*,[27] identify the need of further evolutions to the heterojunction strategy for highly efficient redox photocatalysts and hydrogen generation.

There are various analytical techniques that are being reported to accurately assist in qualifying novel photocatalysts and their photo-physical properties. Amongst which, include ex situ/ in situ irradiated X-ray photoelectron spectroscopy (ISIXPS) and surface potentials measuring. For example, measuring the oxidation state of various elements within a heterojunction pair (i.e., $ZnIn_2S_4/TiO_2$) before and during irradiation of the photocatalyst provides valuable insight into the electronic migrations between two species. Considering $ZnIn_2S_4$ and TiO_2, $ZnIn_2S_4$ has a higher Fermi level and pre-irradiation within a $ZnIn_2S_4/TiO_2$ heterojunction, electrons will migrate from $ZnIn_2S_4$ to TiO_2, therefore ISIXPS data will depict Zn, S, and In species at increased binding energies, meanwhile Ti and O at lower binding energies since electron were accepted from $ZnIn_2S_4$. Whereas, during irradiation, the opposite is true as photogenerated electrons in TiO_2's CB migrate to the VB of $ZnIn_2S_4$.

In 2019, Fu and co. workers[28] approached this opportunity by identifying the limitations of traditional Type-II heterojunctions with the advancements of the Z-scheme to propose the *Step-scheme* (S-scheme) approach to dual-photocatalytic heterojunction systems. Fu and co. workers[28] describe the system whereby two n-type photocatalysts (hereafter recognised as PC I and PC II) are each recognised as oxidative and reductive photocatalysts with different work functions, respectively. The transfer of photo-generated electrons in PC I to the valence band holes of PC II eliminate 'less' redox-active excitons, leaving the valence band holes of PC I and conduction band electrons of PC II to facilitate highly reactive photocatalytic reactions as well as limiting intrinsic charge recombination It is important to recognise that the driving force of charge separation is favoured in the S-scheme heterojunction, since the internal electron field generated between PC I and PC II is created after contact, whereby PC I (oxidative photocatalyst) has a higher work function and lower Fermi level, with PC II contrarily having the opposite photo-physical characteristics of PC I (lower work function and higher Fermi level).

The S-scheme has been proposed to operate as explained by the recent review by Xu *et al.*,[17] Two photocatalysts (noted as reductive photocatalyst [RP] and oxidative photocatalyst [OP], Figure 15) when placed in close contact, experience electron transfers from RP to OP since OP has a lower valence band (VB) and conduction band (CB), as well as a larger work function compared to RP. The resulting grafting promotes the electronic migration and hence an overall internal electric field from RP to OP (Figure 15).

The result of creating the internal electric field enhances the electron transfer across the OP/RP interface ((Figure 15c), essentially allowing both Fermi levels of OP and RP to bend and equalise; therefore, recombination of the lower energy CB electrons in OP combine with the lower energy VB holes in RP.

Previously noted in this review,[26] zeta (ζ) potentials were important parameters to consider when constructing heterojunctions. Fu *et al.*,[28] observed such properties of a WO_3 and *g*-C_3N_4 couple. At pH 4, WO_3 nanosheets($\zeta = -22.8$ mV) and *g*-C_3N_4 nanosheets($\zeta = 10.3$ mV). The larger zeta potential value (WO_3 at $\zeta = -22.8$ mV) correlates the increased dispersion of the WO_3 material in the solution, which was an important consideration for grafting onto *g*-C_3N_4 upon construction of the heterojunction system.

Therefore with two photocatalysts of strongly negative and positive zeta potentials, both with differing work functions (see

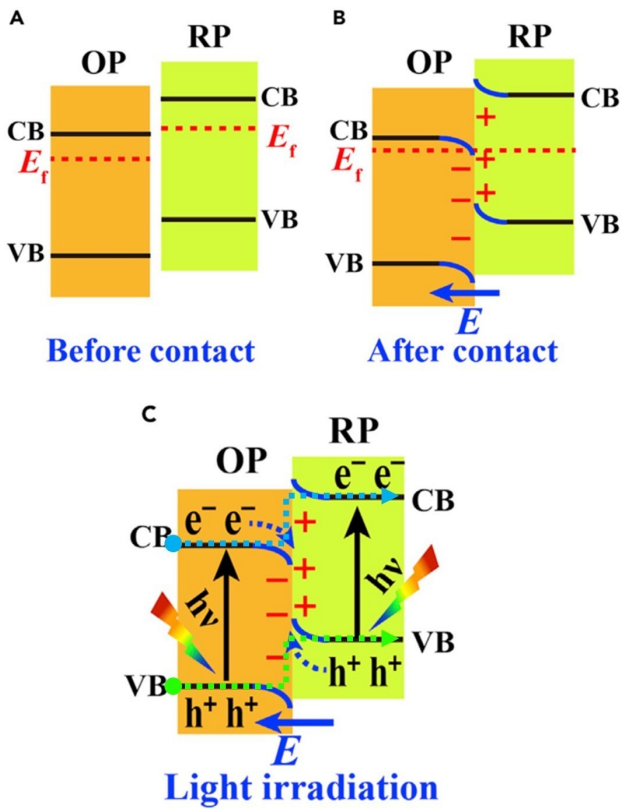

Figure 15. Proposed mechanism of S-scheme heterojunction photocatalysis.[17] An internal electric field is created after contact (B) and through Fermi level alignment post-contact, the "step" configuration is presented (C). Adapted with permission from Ref. [17] Copyright (2020) Elsevier.

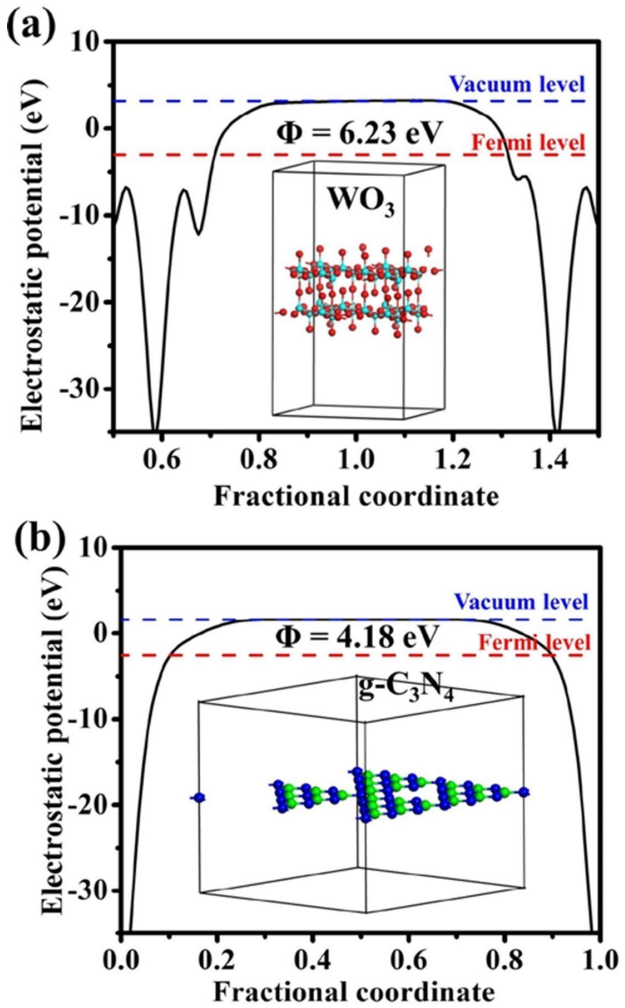

Figure 16. Density functional theory (DFT) calculations of the electrostatic potentials for the (001) surfaces of WO_3 (left) and *g*-C_3N_4 (right). Adapted with permission from Ref. [28] Copyright (2019) Elsevier.

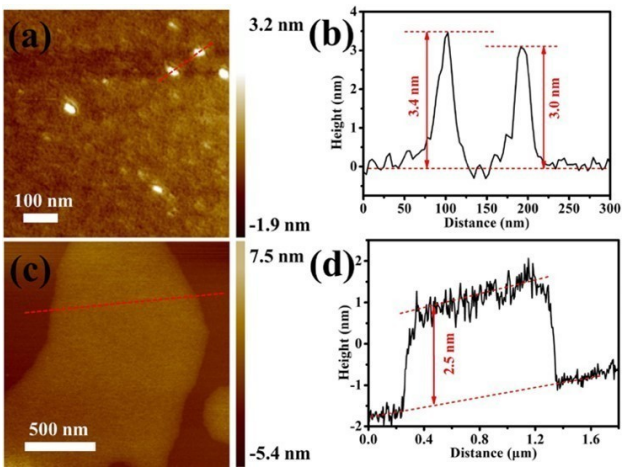

Figure 17. AFM lateral size imagery (image a and c) of WO_3 and *g*-C_3N_4 nanosheets, and particle size thickness, respectively. Adapted with permission from Ref. [28] Copyright (2019) Elsevier.

for example Figure 16 of WO_3 and *g*-C_3N_4), WO_3 and *g*-C_3N_4 could tightly graft forming WO_3/*g*-C_3N_4 nanosheets. The electrostatic zeta repulsion of both photocatalysts (exemplary reference to PC I and PC II) favoured enhanced reductive and oxidative processes, while the value of the work functions (WO_3, $\varphi = 6.23$ eV and *g*-C_3N_4, $\varphi = 4.18$ eV) lend support when understood with the zeta potentials.

In order to validate the construction of the postulated S-scheme heterostructure, Fu and co. workers[28] utilised atomic force microscopy (AFM), XPS and TEM analyses to help identify the existence of the bonding between WO_3 and *g*-C_3N_4 (Figure 17).

Figure 17 has depicted size characterisation of both WO_3 and *g*-C_3N_4. Lateral WO_3 particle sizes were typical of 50–100 nm, with nominal thicknesses between 3–4 nm. In conjunction with HRTEM imagery, lattice fringes were observed and reported as 0.377 and 0.365 nm, corresponding to the (020) and (200) lattice fringes of monoclinic WO_3. Similar practises were completed for *g*-C_3N_4, and 2.5 nm thick wedges of *g*-C_3N_4, consisting of layers exceeding 500 nm were identified. Yet, to explore the coupling of WO_3 and *g*-C_3N_4, HRTEM imagery of 15% WO_3 on *g*-C_3N_4 (15%WO_3/*g*-C_3N_4) revealed strong interfacial contoured contact between both WO_3 and *g*-C_3N_4 (Figure 18).

The red circled regions of Figure 18 (left), were identified as WO_3 nanosheets based on previous particle size calculations and Figure 18 (right) was used to depict the strong interfacial binding between WO_3 and *g*-C_3N_4. Once the bonding between nanosheets of WO_3 and *g*-C_3N_4 was confidently observed by the authors,[28] they investigated hydrogen production over 15% WO_3/*g*-C_3N_4. Un-altered nanosheets of *g*-C_3N_4 were capable of producing gaseous hydrogen (H_2) due to its intrinsically high CB positioning, hence strong reduction potential (583 $\mu mol\, h^{-1} g^{-1}$), whereas nanosheet WO_3 was incapable of H_2 production due to its low CB position. However, after coupling and inducing charge separation through the development of a S-scheme band alignment, 15%WO_3/*g*-C_3N_4 was highly efficient at producing 982 $\mu mol\, h^{-1} g^{-1}$.

The discovery and advancement of the S-scheme heterojunction is indeed a significant improvement in preventing exciton recombination for heterogeneous photocatalysis. Bootluck and co. workers[29] have discussed α-Fe_2O_3/TiO_2 with palladium nanoparticles for photocatalytic hydrogen production, whilst using BET analysis, photoluminescence spectroscopy, EDS and microscopy to characterise the S-scheme. Zhen *et al.*,[2m] have explored a novel S-scheme *g*-C_3N_4/Bi_2MoO_6 heterostructure for phenol degradation studies under visible light irradiation. The vast extent of the literature pertaining to the S-scheme is beyond the scope of this article. However, there are a plethora of excellent reviews detailing the recent advancements of S-scheme photocatalysis reported by the scientific community.[17,27,30–32]

With an understanding of developing heterojunctions across two semiconductor interfaces and the evolution through conventional Types I, II, and III alignments, Z-scheme and recently, the S-scheme, the proceeding text has explored the significance of developing Schottky barriers between metal

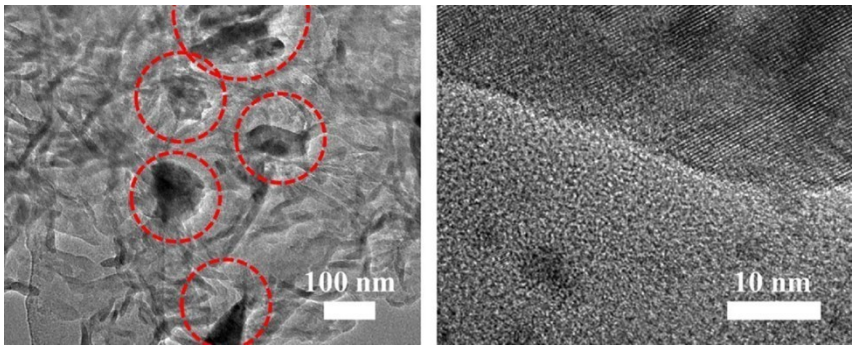

Figure 18. HRTEM micrographs of 15 %WO_3/*g*-C_3N_4. The high contrast red-circled regions depict WO_3 bound to *g*-C_3N_4. Adapted with permission from Ref. [28] Copyright (2019) Elsevier.

nanoparticles and semiconductors. Noble metals offer the unique contribution to semiconductor-mediated photocatalysis through absorption of itinerant electrons *via* harnessing of the metal's electronic cloud, known as surface plasmon resonance and furthermore, with the introduction of intrinsic non-metal counter ions of metal chalcogens, photo-catalysts can be highly efficient in mediating photo-chemical pro-cesses, as described below.[33]

1.5. Metal and Non-Metal Functionalisation Strategies of Semiconductors

In this chapter, metal and non-metal functionalised semiconductors are discussed. The characteristics (enhanced visible light reactivity, reduced band gap and improved charge separation) imparted to metal chalcogens (chalcogens refer to group 16 elements) after being doped generate characteristic alterations to the band structure and by the use instrumental methods, the amalgamation of inherent properties to the metal oxide and the external dopant bring new photo-physics that drive specific photocatalytic-tasks.

Both metal and non-metal ions are commonly reported in the literature as doping agents, which are shown to attenuate the light activating properties of semiconductor materials through either surface or bulk attachment scenarios. This project, however, will explore (with reference to Scheme 1), the *how* and *why* doped semiconductors accomplish higher photocatalytic activities. This has been addressed by studying the instrumental techniques used to probe the doped semiconductor species.

1.5.1. A Brief Understanding of Metal-Doping Nano-Morphology Coupled to Spectroscopic Responses

Over the past decade, silver, gold, and platinum (Ag, Au, and Pt) have received in-depth photocatalytic investigations due to their ability to enhance photocatalysis reactions through intrinsic surface plasmon resonance properties.[34–36]

The surfaces' of adsorbed species (metallic Ag, Au or Pt) experience an enhanced photo-response in the electromagnetic field, which arises from the contact between the metal nanoparticle and the adsorbent's surface (*i.e.* titanium dioxide).[37] Furthermore, when the nanoparticles are within close proximity to the adsorbent's surface, they induce a plasmonic resonance to the surrounding particles with a synergistic effect of a dipole-dipole relationship existing between nanoparticles.[38] During the irradiation period, the synergy between a dielectric medium and metallic nanoparticles (which function as radiating antennae) mounted on the support is capable of creating a photoelectrical excitation in response to wavelength energies that match the unique radius of the nanoparticle.[39]

Coupling metallic nanoparticles and an electromagnetically activated metal oxide produce a solid-state material capable of 'visible-light-driven' photocatalytic functions (oxidation and reduction reactions). The selection of metal nanoparticle (silver or gold) either favours ultraviolet (UV) or visible light activation, respectively, and are highly dependent on the size and shape of the nanoparticles.[40]

Studies have shown that controlled morphological growth of noble metal nanomaterials (size and shape [prisms, rods, spheres]) and monitoring preparation temperatures greatly affect the plasmonic wavelength's absorbance response.[37,41,42]

In a positive ion background, the collection of a metal's conduction electrons simultaneously oscillate, which is then utilised to infer various geometric and sizes of the metallic nanostructures.[43] The dimensions and various shapes (for example, silver [Ag] nanoparticles) have significant effects on the optical absorption of incoming radiation (Figure 19).

Arising from variations in nanocrystalline shapes, Figure 19 has depicted how extinction, scattering and absorption maxima of various silver nanoparticulates vary. Upon light exposure of silver particles, the spheres (for example), experience dipole moments with the same frequency, yet opposite dipole sign to the incident light. Furthermore, as a result of incident light energy loss, a non-uniformity in the quadrupole arises, thus developing shoulder peaks in the spectra (see Figure 19 [a]); 410 nm with strong quadrupole resonance and 370 nm with weaker [shoulder peak] quadrupole resonance).

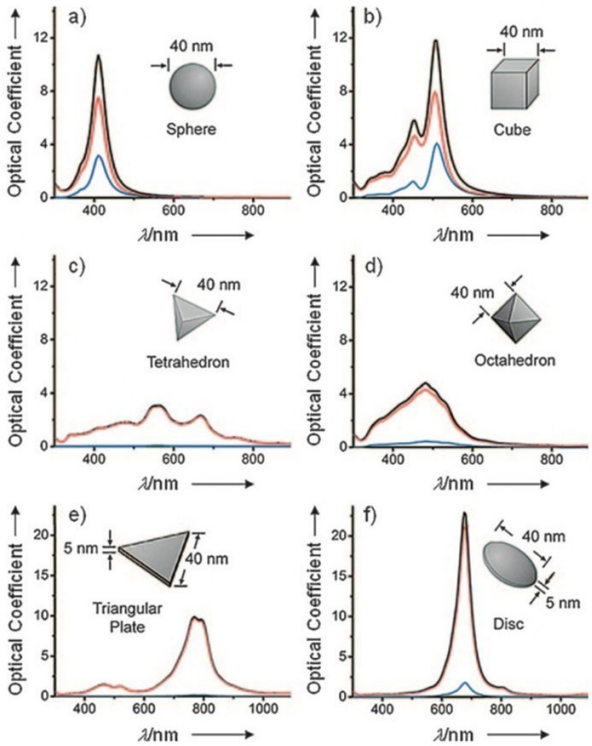

Figure 19. Various silver nanoparticles with their respective absorption maxima as an effect of their varying dimensionalities. Scattering spectrum (blue), extinction (black) and absorption spectrum (red). Adapted with permission from Ref. [43] Copyright (2013) Springer Nature.

Images b-f of Figure 19 have depicted various shape structures of various silver nanoparticles and how physical dimensions may affect the outcome of developed multi-component photocatalysts. In a related text, de Jesus *et al.*,[44] provided a detailed review of the intrinsic properties of Zn_2GeO_4 (ZGO). The various photo-physics and fabrication approaches on the effect of physiochemical responses to size and morphological differences were discussed. de Jesus *et al.*,[44] neatly summarised how the choice of preparation techniques (coprecipitation, hydrothermal or sol-gel) can vastly alter the absorption maxima of ZGO's from ~540 up to 650 nm for rod shaped ZGO-based metal oxide species. Furthermore, the creation of sub-band gap conduction and valence band defects have been reported for controlled photochemical redox applications using ZGO microwires and micron-rods.[45,46]

Non-metal species also offer the possibility to alter the band structure of semiconductors. In the process, extending exciton lifetimes, reducing electron-hole recombinations and attenuating away from ultraviolet light activation are all possible.[47,48] These will be discussed later on in greater detail after reviewing how metals interact with a photocatalyst at the electronic level.

1.5.2. Overcoming Photo-physical Overpotentials of Multi-component semiconductor systems using Band Bending Schottky Barriers

When a semiconductor is functionalised with a noble metal and exposed to a visible light source ($\lambda \geq 420$ nm), intraband electron excitations occur (examples include: Ag: 4d→5sp; Au: 6sp→sp conduction band (CB) (principal quantum number was not defined) and Pt: 5d→6sp conduction band).[49,50] Preceding the photo-activation of the nanoparticle, electron transfer into the conduction band of the metal oxide support resolves two redox processes simultaneously. The freely available positive holes in the metal nanoparticles are capable of performing alcohol oxidations, as graphically summarised below (direct photocatalysis, Figure 20, Path **a**); meanwhile the electrons transferred to the metal oxide's conduction band are captured by a terminal electron acceptor (molecular oxygen for example), whereby the production of superoxide radicals act as secondary oxidising agents for alcohol oxidations (indirect photocatalysis, Figure 20, Path b).[51]

However, to ensure an efficient synergy between metal nanoparticle and metal oxide support, the 'Schottky Barrier' (denoted as Φ_B in Figure 21) formed between the metal/semiconductor junction needs to be assessed (Figure 21).[50]

Sufficient energy to overcome the Schottky Barrier is required for electron ejection from the metal (dopant species) into the conduction band of the chosen semiconductor as the Schottky Barrier causes a large interfacial charge transfer resistance (overpotential). After the Schottky Barrier has been surpassed, electron ejection and hence exciton recombination quenching occurs due to the limited back electron transfer.

Three physical parameters (Schottky Barrier [Φ_B], work function$_{metal}$ [W_{metal}] and electron affinity$_{semiconductor}$ [E_{EA}]) govern how successful a metal functionalised semiconductor system proceeds.

After creating an interface between a semiconductor and a metal ion (refer to Scheme 1), orbital band bending between the semiconductor and metal occurs due to a compulsory dipole field effect at the semiconductor-metal boundary. For an electron to be subsequently transferred from the metal to the semiconductor, the height of the Schottky Barrier (Φ_B) must be

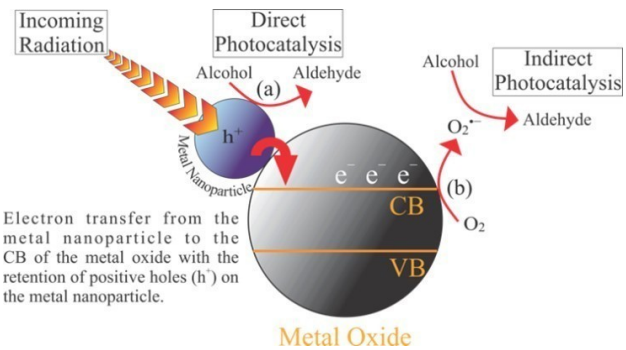

Figure 20. Sketched representation of the dual component action of photo-redox chemistry on semiconductor surfaces *via* direct (a) or indirect (b) photocatalytic routes.

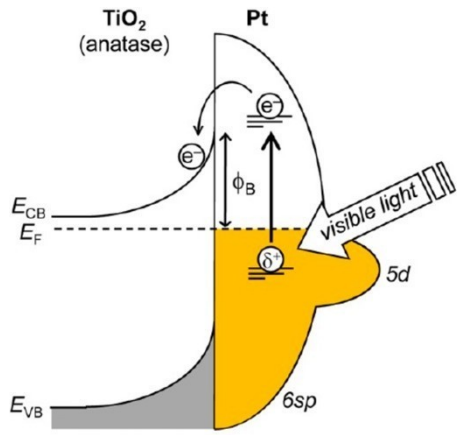

Figure 21. Schottky Barrier existence across platinum and titanium dioxide's surface. Once the Schottky barrier is overcome, electrons (e^-) from platinum relax into the conduction band (ECB) of TiO_2. Adapted with permission from Ref. [50] Copyright (2013) American Chemical Society.

overcome. The Schottky Barrier is defined as the difference of the metal's work function ($W_{metal,}$ energy requirement to remove an electron from the metal's surface to vacuum) and the electron affinity of the semiconductor (E_{EA}, the accumulated energy gathered after an electron positioned within the vacuum level of the semiconductor moves to the conduction band). In-depth knowledge of Schottky Barriers has been well reported in the physics domain.[52–54]

The area of field effect transistors (FET) is beyond the scope of this review. However, in 2016, Kim *et al.*[55] published details of a metal oxide semiconductor field effect transistor (MOSFET) with n-channel germanium. Relevant information within their research was noted to pertain to this review on heterogeneous semiconductor mediated photocatalysis. They noted while attempting to construct a titanium-germanium contact that Fermi level pinning and a large Schottky Barrier were formed. To overcome the restriction induced by the Schottky Barrier, which was impeding electron flow between the metal contact and germanium surface, a metal-interface-semiconductor film was introduced to remediate this limitation. The metal-interface-semiconductor was tested after the introduction of an optimal 2 nm TiO_2 film between the Ti and Ge surfaces (Figure 22).

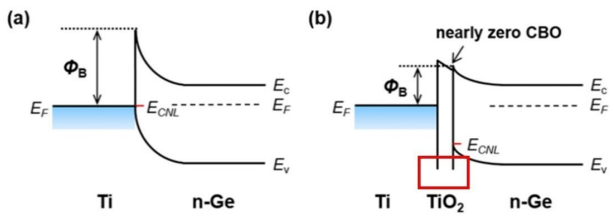

Figure 22. Insertion of TiO_2 film in-between the Ti/Ge films to lower the Schottky Barrier. Adapted with permission from Ref. [55] Copyright (2016) American Chemical Society. (Note, CBO above: 'Conduction band offset').

The TiO_2 semiconductor thin film was noted to drastically reduce the Schottky Barrier height (Figure 22 [image b]) due to the relaxation of the Fermi level of titanium towards the charge neutrality level (Note E_{CNL} in Figure 22) that arose from the near proximity to its conduction band edge. Furthermore, the authors identified that the addition of a 1 nm thick GeO_2 layer introduced a perfect ohmic contact between the Ti and *n*-Ge layers. Introducing foreign doping layers has the potential to significantly enhance the photoelectron-capacity of dual-metal-components photocatalysts as described by Cheng *et al.*,[2n] who investigated the introduction of nickel (as a non-noble metal plasmonic species), with strong visible light absorption capabilities.

An abundance of hot electrons was made available from Ni in conjunction with sulfur vacancies to dope two $Mn_{0.3}Cd_{0.7}S$ species (MCS-s [sulfur rich vacancies] and MCS-p [sulfur poor vacancies]) in a hydrogen photoreduction methodology (Figure 23).

Cheng *et al.*,[2n] explored the possibility to enhance the photoreductive hydrogen potential of $Mn_{0.3}Cd_{0.7}S$ catalysts using nickel as a co-catalyst and seawater as the host's reactant for manufacturing the important green-energy fuel. During Cheng and co. workers'[2n] investigations, preliminary studies using undoped $Mn_{0.3}Cd_{0.7}S$ (MCS), which was prepared via a solvothermal method (as reported elsewhere[56]) only produced

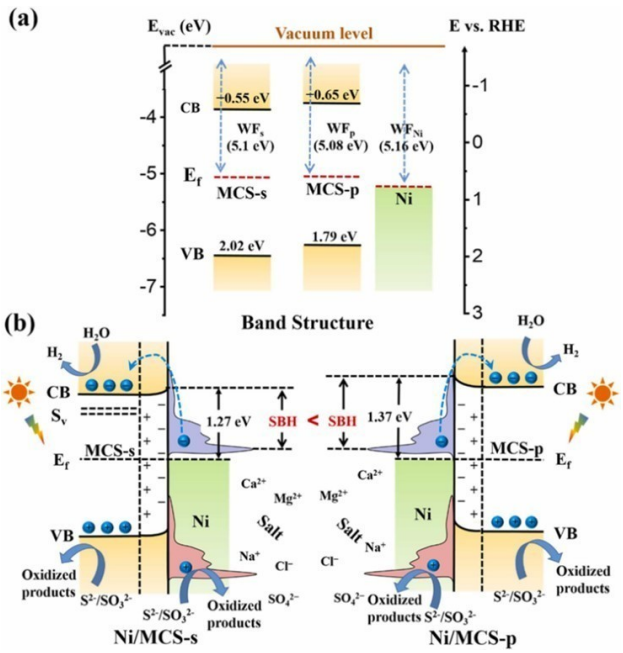

Figure 23. Proposed photocatalytic mechanism of Ni/MCS-s and Ni/MCS-p photocatalysts for the evolution of hydrogen from seawater. Mechanistic pre-coupling of Ni to MCS-s and MCS-p develop a Schottky Barrier at 2 and 3. The presence of sulfur vacancies on Ni/MCS-s lower the Schottky Barrier Height (SBH, 2), while MCS-p with fewer s-vacancies has lesser SBH reduction (3). Reduction of water to molecular hydrogen occurs (4), meanwhile the presence of cationic species (Ca^{2+}, Mg^{2+} and Na^+) in sea water promote exciton separation from nickel plasmonic induced electron-hole pairs, therefore enhancing electron migration from nickel and increasing photocatalytic hydrogen production (5). Adapted with permission from Ref. [2n] Copyright (2022) Elsevier.

limited gaseous hydrogen values, MCS-p (1.9 mmol/h/g) and MCS-s (2.4 mmol/h/g). After incorporating sulfur vacancies and a nickel co-catalyst, the outcome changed significantly (1.5 wt% Ni/MCS-s = 164.1 mmol/h/g).

With reference to the proposed mechanism in Figure 23, the authors explained that sulfur vacancies (included through the method of preparation – solvothermal method), produce positively charged centres on the photocatalyst's surface, forming surface states in the band gap and that consequently affect the interfacial charge and therefore charge-space region within the band gap structure of MCS. This led to a decrease in the conduction band's reductive height around the semiconductor interface, tuning the Schottky Barrier and therefore facilitating easier transboundary electron movement. Once loaded with sulfur vacancies, MCS-s nanorods were doped with non-noble amorphous nickel (Figure 24).

Ni/S vacancy rich $Mn_{0.3}Cd_{0.7}S$ (Ni/MCS-s) nanorods were prepared via a photo-induced deposition method and effectively produced the highest reported H_2-production at 164.2 mmol H_2 mmol/h/g in simulated sea water (3.5 wt% NaCl). The Ni^{2+} ions were attached through electrostatic attraction, whereby Ni^{2+} was converted to a nickel layer during *in-situ* photo-reduction. Nickel (as a non-noble metal) was considered important to the photocatalyst study since, it created a Schottky Barrier with MCS, thus inhibiting exciton recombination. Despite nickel being a non-noble species, it exhibits strong light absorption and therefore produced numerous hot electrons during irradiation.

As the authors[2n] were capable of producing nickel at 1–2 nm thicknesses, the metal exhibited supermagnetism, which produced strong electron spin resonance (ESR) signals. The enhanced ESR signals indicated that significant free vacancy sites were being generated within the three-components (Ni, S-vacancies and MCS system). Enhanced vacancy production made MCS more positively charge centred on the surface and resulted in an overall improvement in electron-hole pair separation.

The newly fashioned 1.5 wt% Ni/MCS was examined with powder diffuse reflectance spectroscopy (DRS), which identified how the addition of amorphous nickel have consistently raised the visible light absorption capacity of MCS-s from 500–800 nm (Figure 25a).

When coupled with nickel, a boosted creation of photo-generated electrons into the sulfur vacancy (sub-conduction band level) sites occurs, as observed in the photoelectrochemical measurements (Figure 25b) were strongly evident with an optimal Ni-loading being 1.5% as noted by the purple peaks. Interestingly, was the observation reported that the Ni-amorphous layer was more effective that platinum, a well-recognised hot-electron standard (Figure 25c). The electro-

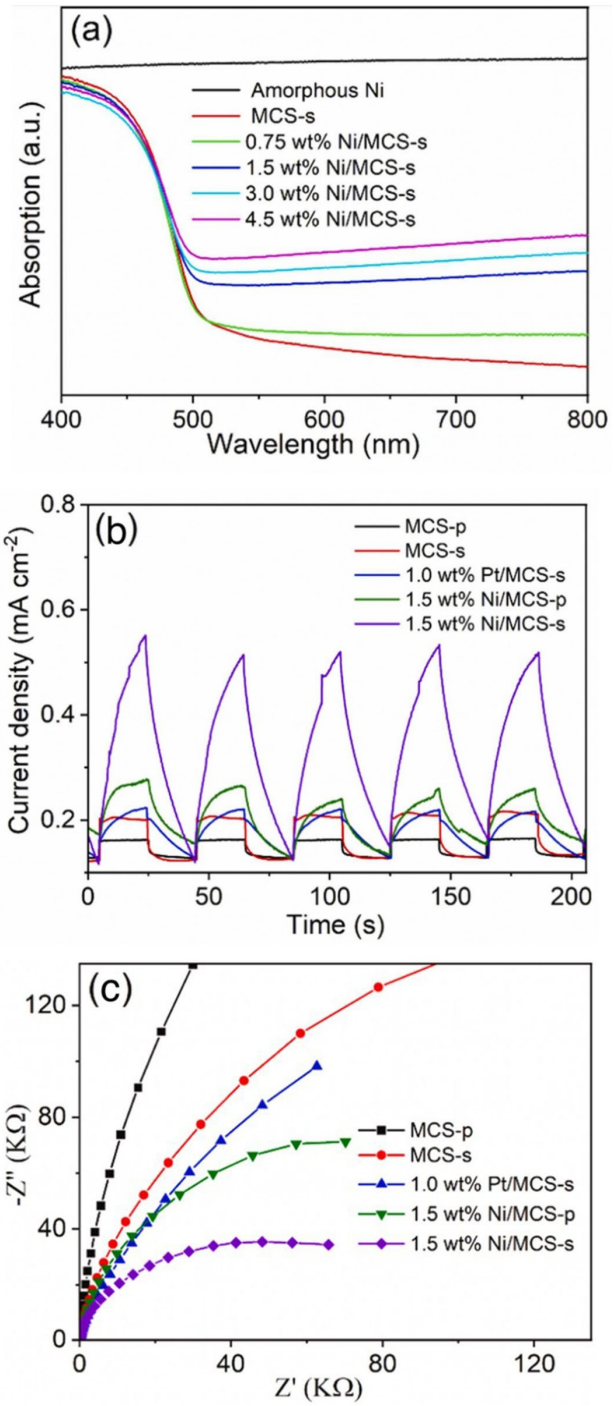

Figure 25. Spectroscopic review of MCS-s using analytical techniques. (a) Powder diffuse reflectance spectroscopy, (b) photoelectrochemical measurements, (c) EIS Nyquist plots comparing Pt- to Ni- based MCS-s. Adapted with permission from Ref. [2n] Copyright (2022) Elsevier.

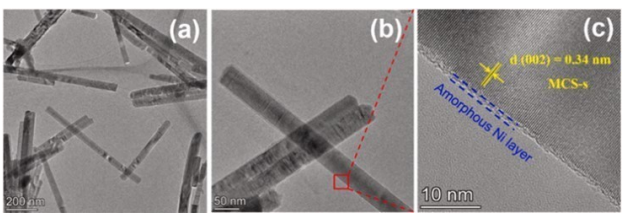

Figure 24. Amorphous layer of Ni on the surface edges of MCS-s. The reported lattice fridge d(002) = 0.34 nm corresponded well to MCS-s. The reported thickness of amorphus Ni was 1–2 nm. Adapted with permission from Ref. [2n] Copyright (2022) Elsevier.

chemical impedance spectroscopy (EIS) Nyquist plots have validated how 1.5 wt% Ni/MCS-s was more significantly more efficient at decreasing interfacial charge-transfer resistance across the Schottky Barrier than 1.0 wt% Pt/MCS-s (Figure 25c).

Cheng *et al.*,[2n] have been able to successfully demonstrate after the addition of an amorphous film of nickel onto the surface of MCS-s that the intrinsic sulfur vacancies provided a symbiotic-like relationship towards the incoming hot-electrons of nickel, whereby favouring hydrogen photoreduction and co-currently inhibiting salt corrosion in sea-water by absorbing cationic species (such as Na^+, Mg^{2+} and Ca^{2+}).

Sulfur-based photocatalysts are known to be vulnerable to redox process and hence loss in activity through oxidation of sulfur (for example CdS to CdO).[2h,i] Yet, as demonstrated in the works by Cheng *et al.*,[2n] sulfur is indeed a valuable species in heterojunction synthesis for its valuable contribution to catalysis. Furthermore, metal sulfide semiconductors have proven successful in photocatalytic activities due to their high energy-harvesting capacity to absorb visible light and promote excellent exciton generation and separation.[57] For this reason, intrinsic sulfur based photocatalysts and sulfur doping reports are elaborated below.

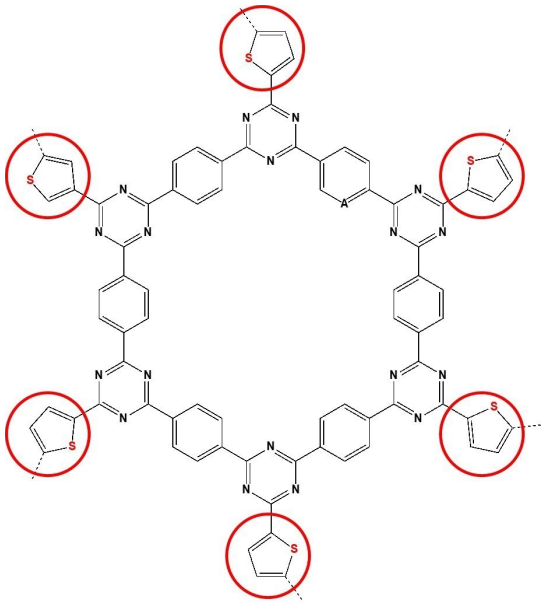

Figure 26. Thiophene based CTFs. Red circles depict the sulfur moieties bound to the CFTs.

1.5.3. Non-Metal Doping Photocatalysts Inducing Attenuated Band Gap Structures

Liao *et al.*[2a] investigated the photo-application of introducing sulfur as a non-metal dopant (through thiophene moieties) into narrow band-gapped covalent triazine frameworks, *CTFs* (consisting of aromatic C=N linkage) for benzylic alcohol derivative oxidations over traditional phenyl-based CTFs. The photocatalytic system (thiophene structured CTFs) is not directly aligned to the nature of this review, being focused on heterogeneous metal-oxide semiconductors, however, the instrumental techniques applied by Liao *et al.*[2a] neatly describe interesting observations (Figure 26).

Including thiophene rings into the covalent triazine frameworks allowed for superior benzylic alcohol oxidation conversions (up to 285% increase) over traditional phenyl-based CTFs. Sulfur was identified through UV-Vis diffuse reflectance spectroscopic data (Figure 27) to optically shift the band gap potentials of phenyl-based CTFs to thiophene-based CTFs by 0.5–1.06 eV.

Furthermore, thiophene-based CTFs produced lower energy band gaps, hence driven by lower energy electron migrations to the respective conduction bands that were activated by 500 nm irradiation. Not only did sulfur lower the respective band gaps of phenyl-based CTFs but also efficiently enhanced the electron mobilities from within the band structure of the CTF's π-conjugation. This was measured using electron paramagnetic resonance (EPR) spectroscopy, as depicted in Figure 28 below.

On the topic of sulfur, Su and co. workers[2b] developed a heterojunction (TC/N-ZIS) between layered $Ti_3C_2T_x$ and ultrathin N-$ZnIn_2S_4$ that was subsequently utilised for the application of hydrogen production from splitting water. Interestingly, after determining zeta potentials of each component (nano-sheet N-

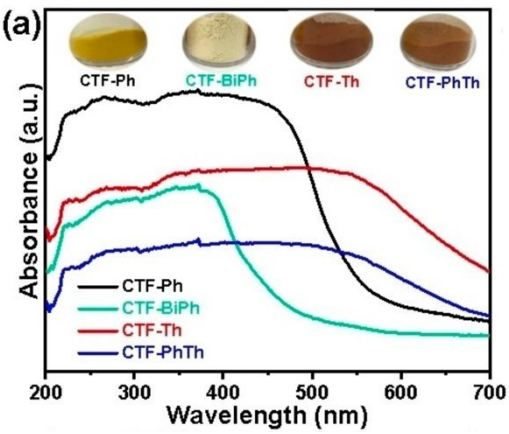

Figure 27. Band structure altering of covalent-triazine-frameworks through thiophene moiety doping. Note; CTF–Ph (phenyl) and CTF-BiPh (biphenyl) refer to phenyl based CTFs, while CTF-Th and CTF-PhTh refer to thiophene-based CTFs. Adapted with permission from Ref. [2a] Copyright (2020) John Wiley and Sons.

$ZnIn_2S_4$ @ −39.8 mV and $Ti_3C_2T_x$ @ −31.8 mV), the authors[2b] introduced NH_4^+ (as NH_4HCO_3) as a binder to alter the homogeneous state of both species ($Ti_3C_2T_x$ and ultrathin N-$ZnIn_2S_4$) that induced precipitation of the two-component compounded TC/N-ZIS semiconductor system. The inclusion of the cationic NH_4^+ species promoted the precipitation and hence created a Type 1 straddling band gap heterostructure (future details in the authors' article[2b]) and protected the well reported oxidisable sulfur of indium-sulfur photocatalysts.[2b,58]

After anchoring $Ti_3C_2T_x$ (co-catalyst) onto N-$ZnIn_2S_4$ to accept electrons from the sulfur-photo-activated sites on N-$ZnIn_2S_4$, the hydrogen-production capacity of TC/N-ZIS reached

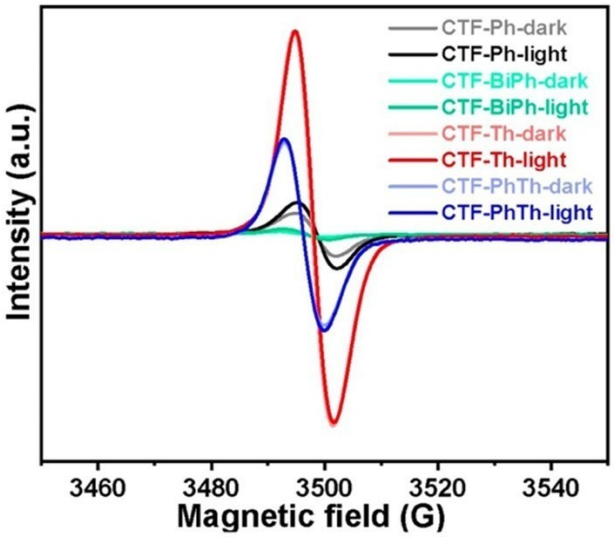

Figure 28. EPR study of two thiophene (Th)- and two phenyl (Ph)- based CTF's. Obtained spectra were collected using UV irradiation and in a dark environment to observe the effect of photo-activation. Note: 'CTF-Th-light' and 'CTF-PhTh-light' responding with the highest electronic intensities arising from non-metal sulfur incorporation. Adapted with permission from Ref. [2a] Copyright (2020) John Wiley and Sons.

H_2 levels of 148.2 μmol h^{-1}. In comparison to the individual constituents, trace hydrogen detection was only observed with $Ti_3C_2T_x$, while $ZnIn_2S_4$ produced hydrogen at 40.7 μmol h^{-1} (Figure 29).

Su and co. workers[2b] explored a comprehensive study to investigate the photo-mechanics and understand the improved photo-reductive capabilities of the TC/N-ZIS composite over the individual components ($Ti_3C_2T_x$ and N-$ZnIn_2S_4$). The capabilities of modern instrumentation were exemplified while investigating and understanding the photo-physics that governed the semiconductor mediated photocatalysis as discussed below. Firstly, Raman spectroscopy was utilised to postulate that carbon species present in $Ti_3C_2T_x$ were responsible for derivatised graphitic carbon in TC/N-ZIS and functioned as an electron tunnelling agent between $Ti_3C_2T_x$ and N-$ZnIn_2S_4$, where electrons were efficiently funnelled to prevent oxidative damage to the sulfide semiconductor (N-$ZnIn_2S_4$, Figure 30).

As observed in Figure 30 above, N-$ZnIn_2S_4$ presented no Raman modes after approximately 350 cm^{-1}, whereas D and G bands of graphitised carbon were present in both $Ti_3C_2T_x$ and TC/N-ZIS. The evidence lead to predict that the carbon species originated from $Ti_3C_2T_x$ due to their pre-($Ti_3C_2T_x$) and post-appearance in the composite semiconductor.

In additional studies to further corroborate the proposed mechanism outlined in Figure 29, electron spin-resonance (ESR) and X-ray photoelectron (XPS) spectroscopic techniques were conducted to probe the newly developed heterojunction. ESR reports (Figure 31, image A) identified strong signals at $g=$ 2.004 for 4-TC/N-ZIS, detecting that strong electron capture was occurring in the heterojunction and the presence of sulfur vacancies were in existence. XPS studies (Figure 31, images B-D) were utilised to further discover sulfur vacancies in N-$ZnIn_2S_4$, as the binding energies of the respective species, Zn $2p_{3/2}$ (1022.06 eV), Zn $2p_{1/2}$ (1045.11 eV), In $3d_{5/2}$ (445.00 eV), In $3d_{3/2}$ (452.55 eV), S $2p_{3/2}$ (161.60 eV), and S $2p_{1/2}$ (162.81 eV) were observed at positively shifted values, which was indicative of electron transfer from N-$ZnIn_2S_4$ to $Ti_3C_2T_x$.

Su and Co. workers further identified a plausible mechanistic understanding of the newly fashioned heterojunction between $Ti_3C_2T_x$ and N-$ZnIn_2S_4$ (Figure 32) after utilising Density Functional Theory (DFT) calculations to predict the work functions (φ) of $ZnIn_2S_4$, $ZnIn_2S_4$ with sulfur vacancies and $Ti_3C_2O_2$ as 4.20, 3.74 and 5.34 eV, respectively. The importance of such information led the authors to understand the nature of electron transfer, which in this case, was an electronic migration from the $ZnIn_2S_4$ species to $Ti_3C_2O_2$ due to the higher eV value of $Ti_3C_2O_2$, which was in accordance with XPS data – negatively

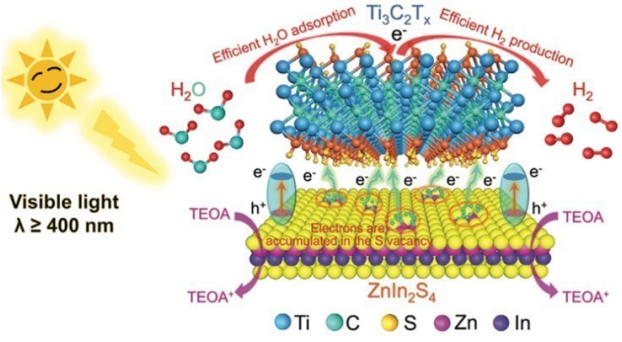

Figure 29. Compound heterostructure between $Ti_3C_2T_x$ and $ZnIn_2S_4$. As observed in Figure 29 above, when the compound semiconductor (TC/N-ZIS) is irradiated with visible light ($\lambda \geq 400$ nm), electrons are excited from $ZnIn_2S_4$ through positive hole migration to the surface and are captured by $Ti_3C_2T_x$, thus in-turn facilitating water reduction. Adapted with permission from Ref. [2b] Copyright (2022) John Wiley and Sons.

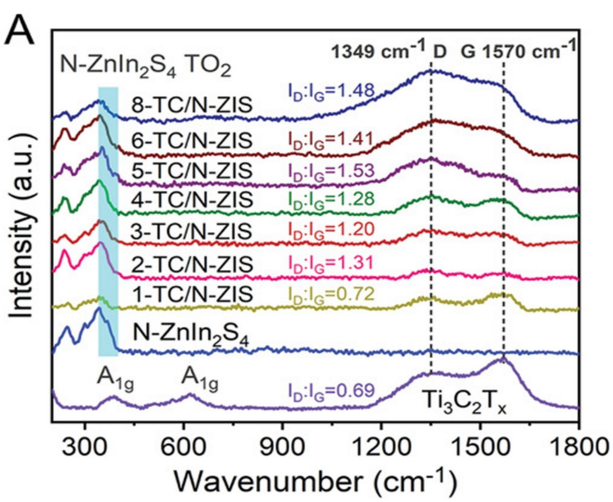

Figure 30. Raman spectra of TC/N-ZIS compounded semiconductor, with varying wt% of $Ti_3C_2T_x$ as denoted by *x*-TC/N-ZIS, where $x=$ 1,2,3,4,5,6 and 8 wt% $Ti_3C_2T_x$. Noticeable are the two peaks at 1349 and 1470 cm^{-1}, indicative of the D and G bands of graphitised carbon, respectively. Adapted with permission from Ref. [2b] Copyright (2022) John Wiley and Sons.

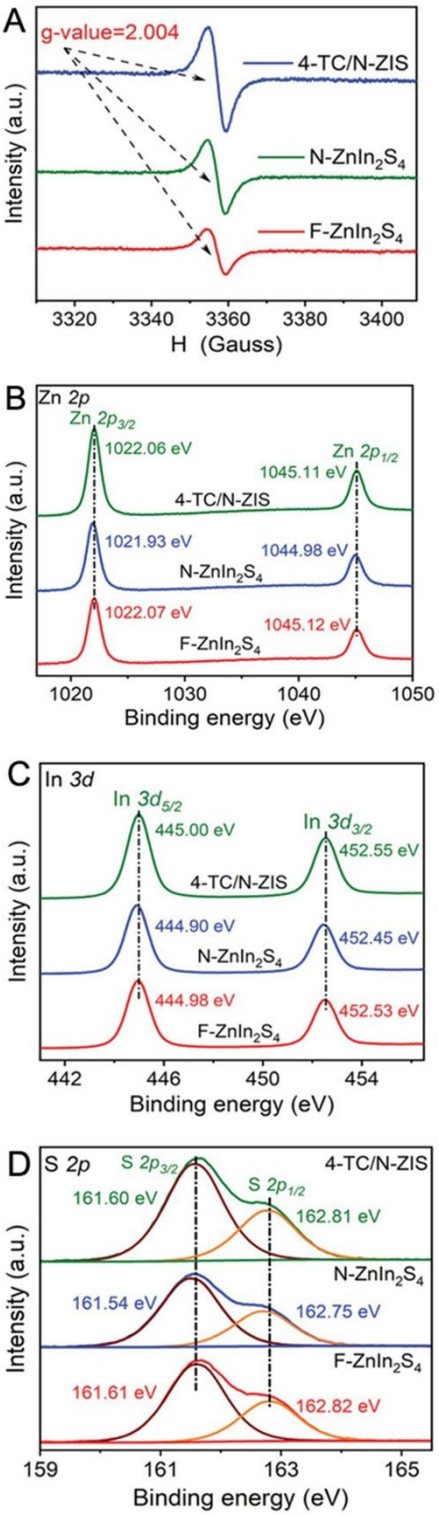

Figure 31. ESR spectra of 4-TC/N-ZIS (image A) and XPS spectra of Zn *2p*, In *3d* and S *2p* (images B–D). The presence of $g = 2.004$ responses (a) for 4-TC/N-ZIS identified the detection of free electron capture sites (sulfur-vacancies) and the positive shift in binding energies (images b-d) revealed an electron transfer across the N-$ZnIn_2S_4$ to $Ti_3C_2T_x$ bridge. Adapted with permission from Ref. [2b] Copyright (2022) John Wiley and Sons.

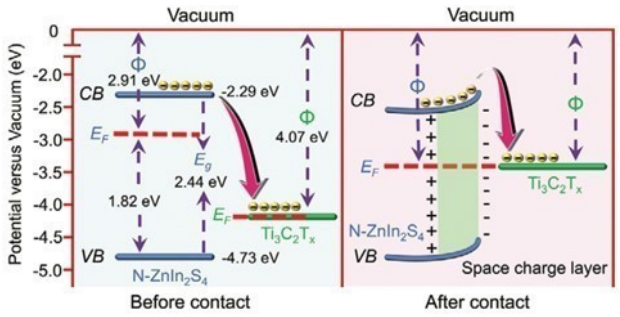

Figure 32. Proposed energy diagram before (left) and after (right) hetero-coupling $Ti_3C_2T_x$ and $ZnIn_2S_4$. Prior to joining both catalysts, the Fermi level of $ZnIn_2S_4$ resided closer to its conduction band, whereas, due to the larger work function of $Ti_3C_2T_x$ the opposite was occurring. Notice the Fermi level of $Ti_3C_2T_x$ located within the valence band. The overall affect was charge migration from the CB of $ZnIn_2S_4$ to $Ti_3C_2T_x$ after contact. Adapted with permission from Ref. [2b] Copyright (2022) John Wiley and Sons.

shifted XPS signals for Zn 2p, S 2p and In 3d indicated a decreased electron cloud over $ZnIn_2S_4$ and therefore more sulfur vacancies. To further understand the electronic migration (and validate the DFT theory) across the $Ti_3C_2O_2$ – $ZnIn_2S_4$ interface (in vacuum), additional ultraviolet photoelectron spectroscopic (UPS) measurements were investigated for the electronic structures of nanosheet $ZnIn_2S_4$ and $Ti_3C_2T_x$. DFT evidence detected the work function of $ZnIn_2S_4$ with sulfur vacancies at 3.74 eV, while $Ti_3C_2O_2$ at 5.34 eV. Discrepancies in the theoretical versus experimental (UPS results for nanosheet $ZnIn_2S_4$ at 2.91 eV and $Ti_3C_2T_x$ at 4.07 eV) values rose from complex surface structures (anomalies and impurities during preparation of $Ti_3C_2O_2$ and $ZnIn_2S_4$ such as –OH, –O and –F surface species).

In accordance with the calculated UPS band structure of N-$ZnIn_2S_4$, the Fermi energy level was closer to the conduction band of N–$ZnIn_2S_4$ than the Fermi level of $Ti_3C_2T_x$. This implied that after forming the $Ti_3C_2O_2$ – $ZnIn_2S_4$ heterojunction interface, photogenerated electrons migrated from the conduction band (CB) of $ZnIn_2S_4$ and into $Ti_3C_2O_2$ that were later used for water reduction (Figure 29).

Detecting foreign atomic doping in the crystal structure of semiconductor species (for example sulfur, graphitised carbon, as reported by Su *et al.*[2b]) reveals observable spectroscopic responses, and hence insight into the extrinsic nature induced upon host materials. Li *et al.*[2c] investigated anatase TiO_2 doped with carbon black for degrading methylene blue. Upon initial characterising using powder diffuse reflectance spectroscopy (PDRS, Figure 33), the addition of low carbon levels (0.2–1.0 %) greatly influenced the visible light spectrum.

Adapted with permission from Ref. [2c] Copyright (2020) American Chemical Society. Available online at https://pubs.acs.org/doi/10.1021/acsomega.0c00504.

Understanding how carbon influenced the potential of TiO_2 to alter the absorbance potential between 400–600 nm required probing the nature of the new photocatalyst microscopically (Figure 34) and if any, atomic lattice changes had occurred.

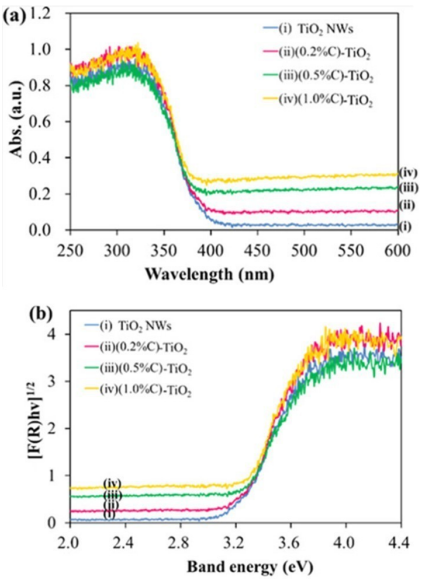

Figure 33. Diffuse reflectance spectra of TiO_2 nanowires (NW), 0.2, 0.5, and 1.0% carbon doped TiO_2, as (0.2%C)-TiO_2, (0.5%C)-TiO_2, and (1.0%C)-TiO_2, respectively (figure a) and determined band energies (eV, figure b).

Without carbon doping, prepared TiO_2 NWs were observed as thin fibrous ±200 nm strands (Figure 34 a,b), whereas upon carbon doping (0.2–1.0% C), the nanofibers shortened to nanorods with multiple particulate dispersions on the rods' surfaces (Figure 34 a,b,c). Observing physical alterations to both the optical absorbance and physical structure of TiO_2 NWs after carbon doping, the authors continued probing the C-doped TiO_2 using Raman spectroscopy and X-ray photoelectron spectroscopy (XPS, Figure 35).

The addition of carbon to TiO_2 NWs caused three major peaks to shift at 135, 488, and 605 cm^{-1} of TiO_2, respectively. Of interest was the height and widths of the 135, 488, and 605 cm^{-1} peaks, as with increasing carbon doping, the peaks broadness and height increased, indicating the inclusion of impurity states, defects (from impurities - carbon), and highly crystalline TiO_2 nanorods. The impurities states were later confirmed with the application of XPS, whereby after increasing the carbon doping percentage (0.2–1.0%), the observed formation of a C 1s (O–Ti–C) peak increased from 5.76 atomic percent (0.2% C–TiO_2) to 9.95% (0.5% C)-TiO_2 and lastly 10.72% (at 1.0% C)-TiO_2. This was noticeable in Figure 35 (bottom, figure a–c) as the peak shoulder at 282.6 eV increased as the carbon doping concentration increased.

1.6. Crystallite Engineering for Alcohol Oxidations with Atomic Detection studies using Spectroscopy and Diffractometry

Carbon doping has further been examined during the photo-oxidation of benzyl alcohol using nanocomposites of graphitic carbon nitride (g-C_3N_4) bound with titanium dioxide. Mohammadi and co. workers[2d] studied the effects of loading titanium dioxide with a non-metal dopant to lower the band gap potential of TiO_2 that facilitated a photocatalytic conversion of benzyl alcohol to benzaldehyde. The authors[2d] claimed, after manufacturing spray-dried g-C_3N_4/TiO_2 granules (using polyvinyl alcohol) that the dual semiconductor composite had a comparably lower energy gap (Figure 36) compared to TiO_2 alone and was the result of carbon doping into TiO_2.

The data depicted in Figure 36 has demonstrated that the inclusion of spray drying g-C_3N_4/TiO_2 lowered the absorbance capacity of TCN, while slightly red-shifting the optical band gap between TCN and TCNg. The authors[2d] however, did not provide comparative data to un-doped TiO_2, which would've been of valuable comparison. Furthermore, the results indicated that TiO_2 was the dominant photo-reactive material as the nanocomposite formed between g-C_3N_4 and TiO_2 strongly represented a typical TiO_2 absorption curve.[59] In addition, the authors identified that the inclusion of g-C_3N_4 into TiO_2 did not influence the configuration of TiO_2 (powder X-ray diffraction analysis, Figure 37.

Whilst the X-ray diffraction peak angles (see article[2d]) were consistent with the individual constituents of TCNg, the optical absorption curves of TCN and TCNg suggest that g-C_3N_4 altered the band structure of TiO_2, rather than TiO_2 doping the crystal structure of g-C_3N_4 as no peak maxima for TCNg was centred at *ca.* 410 nm.

In related studies investigating the adsorption of benzyl alcohol onto the surface of metal hydroxides, Zou and co. workers[2e] preadsorbed benzyl alcohol onto layered double hydroxides (LDH's). The LDH's with the general formula $(M^{II}_{1-x}M^{III}_{x}(OH)_2)^{Z+}(A^{n-})_{z/n}\cdot mH_2O$ consisted of M^{II} and M^{III} as the respective divalent and trivalent cations, while A^{n-} for charge balance of the M-ions in the brucite-like layers. The authors[2e] identified that a 2:1 Zn^{2+}/Ti^{4+} combination in ZnTi-LDH (ZT-2/1) produced the highest number of surface hydroxide sites over other Zn^{2+}/Ti^{4+} ratios at 3:1 and 4:1, and 2:1 was optimal for facilitating the photooxidation of benzyl alcohol under visible light (300 W Xe lamp) conditions.

Studies lead to an interesting investigation that probed the alcohol oxidation mechanism (Figure 38). The layered double hydroxides with a 2:1 ratio of Zn:Ti species prompted the coordination of benzyl alcohol to the LDH's through a high concentration of hydroxides sites that subsequently facilitated the production of oxygen vacancies and within the presence of molecular oxygen, benzyl alcohol was photo-oxidised.

During the authors'[2e] investigation, synthesising the zinc-titanium layered double hydroxide with the ZT-2/1 ratio produced the highest concentration of surface hydroxide sites, which were subsequently proven using multiple techniques (Figure 39).

From Figure 39 the electron paramagnetic resonance (EPR) spectrum (image A) exemplified the $g = 2.004$ signal corresponding to oxygen vacancies present within the ZT-LDH material. BA/ZT-2/1 was identified to possess a signal response significantly larger than either BA/ZT-3/1 or BA/ZT-4/1, whilst ZT-2/1 produced no oxygen vacancy signal, thus indicating benzyl alcohol was mediating the creation of oxygen vacancies upon binding to the surface of ZT-LDH. During additional EPR

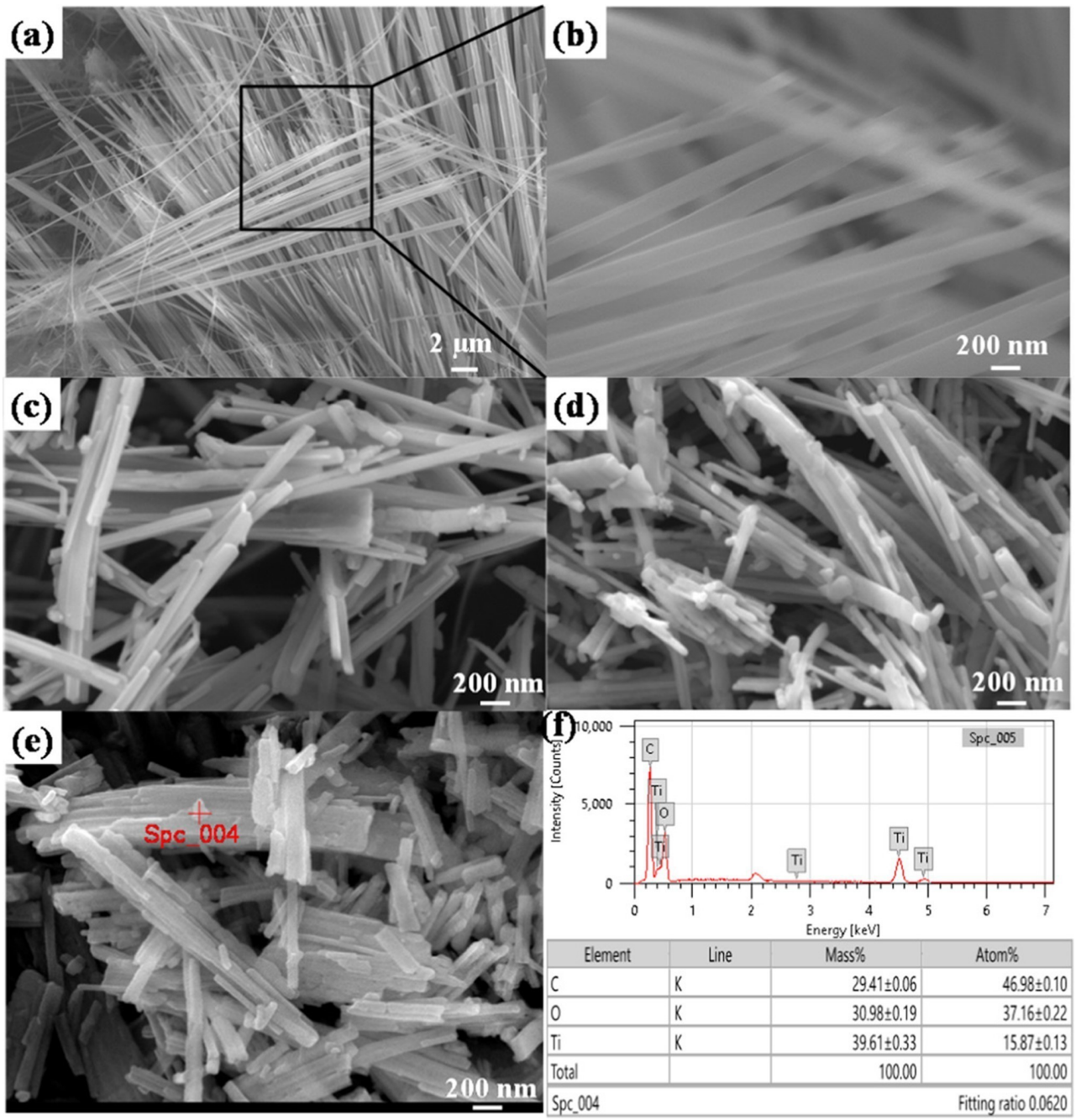

Figure 34. Morphological structure of TiO_2 NWs (a,b), (0.2 %C)-TiO_2 (c), (0.5 %C)-TiO_2,(d) and (1.0 %C)-TiO_2 (E). EDX spectra (1.0 % C)-TiO_2 reported in (f). Adapted with permission from Ref. [2c] Copyright (2020) American Chemical Society. Available online at https://pubs.acs.org/doi/10.1021/acsomega.0c00504.

studies, 5,5-dimethyl-1-pyrroline-*N*-oxide (DMPO) was introduced as a superoxide trapping agent. Similar observations were noted, BA/ZT-2/1 produced the most intense DMPO-OOH signal, indicative of superoxide (O_2^-) ions. Meanwhile without surface coordinated benzyl alcohol, no DMPO-OOH was detected. The data lead to conclude that active site creation was plausible between hydroxide sites and benzyl alcohol.

Subsequent X-ray photoelectron spectroscopy (XPS) studies (images B and C) further suggested that benzyl alcohol was either coordinating through the Ti-specie or the surface hydroxide sites or both; observe a 0.2 eV shift from 458.22 eV to 458.42 eV for Ti-2*p*, 531.3 eV to 531.5 eV for surface hydroxide groups and an additional new peak at 530.2 eV on BA/ZT-2/1, agreeing with the literature of adsorbed molecule oxygen found in vacancy sites on layered double hydroxides.[60,61]

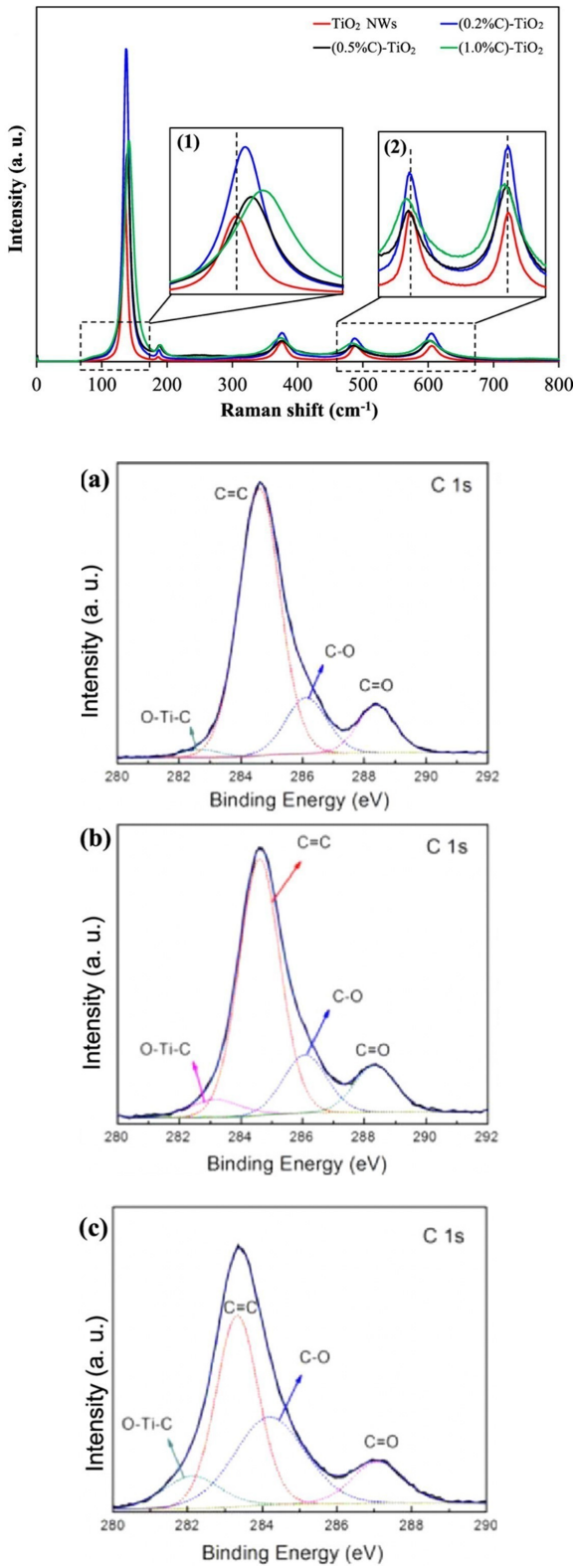

Figure 35. Raman (top) and XPS spectroscopic data (bottom [a-c]). The insets (1 and 2) of the top Raman spectrum magnify the peak shifts of TiO_2 after impurity doping. Reprinted (adapted) with permission from (*ACS Omega* **2020**, *5*, 17, 10042–10051). Copyright (2020) American Chemical Society. Adapted with permission from Ref. [2c] Copyright (2020) American Chemical Society. Available online at https://pubs.acs.org/doi/10.1021/acsomega.0c00504.

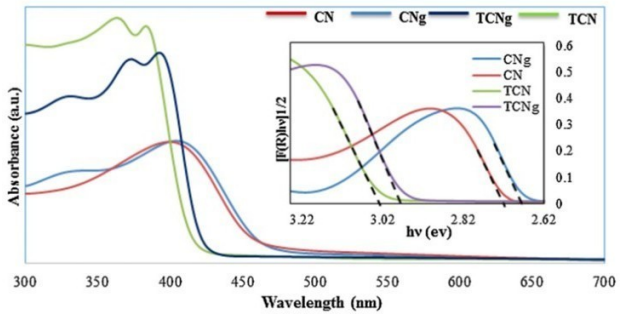

Figure 36. Powder diffuse reflectance data of bulk g-C_3N_4 (CN), spray-dried g-C_3N_4 granules (CNg), g-C_3N_4/TiO_2 nanocomposite (TCN) and spray-dried g-C_3N_4/TiO_2 nanocomposite granules (TCNg). Corresponding Kubelka-Munk plots in the insert. Adapted with permission from Ref. [2d] Copyright (2020) Elsevier.

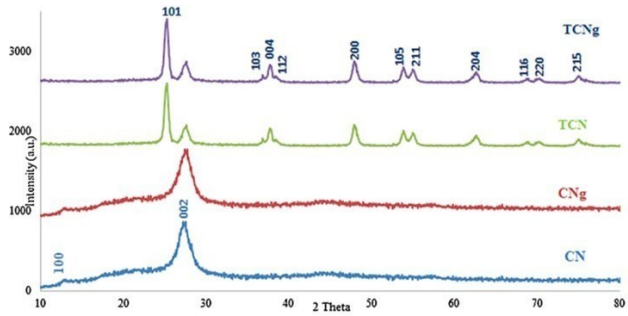

Figure 37. X-ray diffraction analysis of TCNg, TCN, CNg and CN. The diffractograms depict no altering to the configuration of TiO_2 after the doping process was complete. Adapted with permission from Ref. [2d] Copyright (2020) Elsevier.

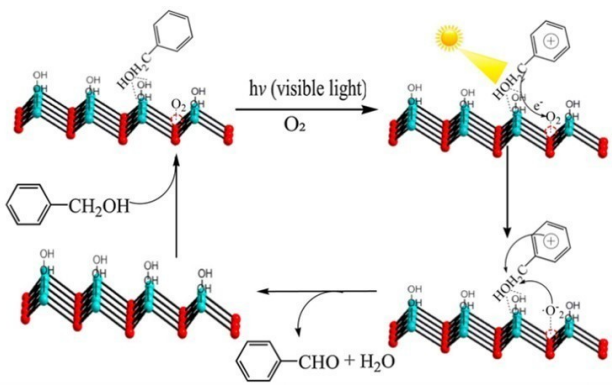

Figure 38. Proposed alcohol oxidation on the surface of ZT-2/1. Coordination of benzyl alcohol to ZT-2/1 through Ti or surface bound hydroxide sites. Post coordination, the deprotonation of the benzyl alcohol molecule through the photo-activated coordination sites would produce carbocationic alcoholic species. Subsequent photo-electron transfer to adsorbed molecule oxygen would in-turn complete the oxidative cycle yielding benzaldehyde and recycled ZT-2/1. Adapted with permission from Ref. [2e] Copyright (2019) Elsevier.

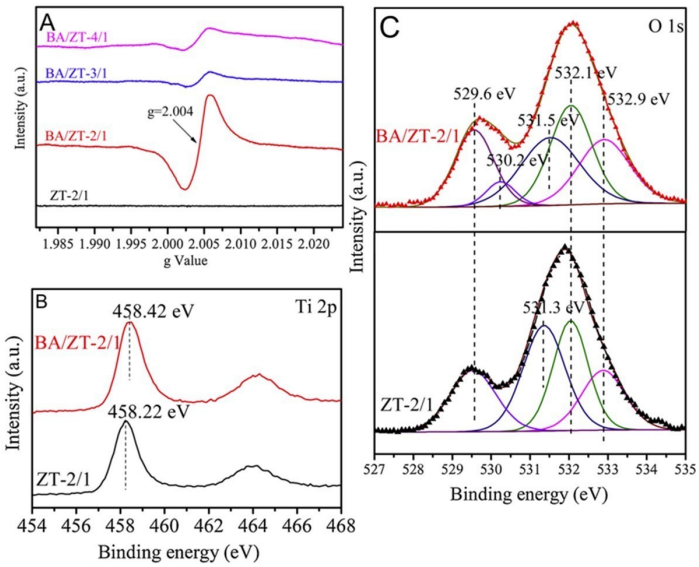

Figure 39. Multiple techniques adopted by Zou *et al.*[2e] that illustrate the capacity of instrumentation to quantify the presence of oxygen vacancies and hydroxide sites on ZT-LDH. ZT-LDH was superior in terms of oxygen vacancy production upon benzyl alcohol surface adsorption (BA/ZT-2/1). Images: image A) EPR spectrum detecting oxygen vacancies. Images B and C) High resolution Ti2*p* and O 1s XPS spectra. Adapted with permission from Ref. [2e] Copyright (2019) Elsevier.

1.7. Surface Loading Semiconductors using Linkers – A discussion of organic dyestuff degradations

Fine-tuning a multi-component semiconductor system towards visible light sensitivity is of great interest to chemists. However, the method of surface loading an organic linker onto a metal oxide requires careful consideration of the nature and exploiting the surface chemistry of the host's surface for efficient organic photodegradation.

Amongst various applications including drug delivery and energy production, metal-organic frameworks (MOF's) have proven highly successful at mediating organic photochemical processes.[62,63] Soliman *et al.*,[64] developed both a hierarchical porous zeolitic imidazolate (ZIF-8) and a ZIF-8 zeolitic imidazolate framework – ZnO nanoparticle-framework structure, loaded with carbon (ZnO@N-doped C) for methylene blue and fluorescein photodegradation (@ 50 mg L^{-1}) studies. ZIF-8 was prepared via a triethylamine-assisted procedure, meanwhile carbonization of ZIF-8 at elevated temperatures produced ZnO@N-doped C.

As previously discussed in this report, zeta potentials have demonstrated great value in catalyst design and application. Upon the research of Abdelhamid and Zou,[65] Soliman *et al.*,[64] capitalised on the positive zeta potential of ZIF-8 nanoparticles (in water, $\zeta => +30$ mV). The high zeta potential of ZIF-8 demonstrated that the opportunity existed for a strong organic compound interaction. Therefore, the authors'[64] investigated the photo-degradation studies of ZIF-8 using methylene blue and fluorescein. However, ZIF-8 has a reported large band gap of ~5.0 eV, thus making it not conducive for semiconductive purposes under visible light irradiation.[66] Therefore, the band gap was attenuated towards ZnO, with a favourably lower band gap, which enhanced excitonic separation for dye degradation studies (Figure 40).

Figure 40 has depicted the contribution of the pre-loading (adsorption) period (0-250 minutes) of the interaction between ZIF-8, ZnO@N-doped C and the respective organics, methylene blue and fluorescein. Comparably low levels of organic dye degradation/ media adsorption (and ultimately removal from solution) were minimal when compared to the photodegradation period (250–500 minutes). Evidently, why was the efficiency of both ZIF-8 and ZnO@N-doped C towards methylene blue more effective at photo-mineralisation over fluorescein?

Zeta potentials of ZIF-8 were identified as highly positive ($> +30$ mV), thus indicating the ZIF-8 zeolitic imidazolate framework – ZnO nanoparticle-framework structure (ZnO@N-doped C) was positively surface charged. Secondly, analysing the XPS spectra revealed three investing observations. Firstly, XPS Zn 2p spectra revealed no oxidation state shifting in the Zn $2p_{3/2}$ (1044.9 eV) and Zn $2p_{1/2}$ (1021.9 eV) peaks. Therefore suggesting no electron loss or gain of zinc after organic dye adsorption. Secondly, after carbon peaks were deconvoluted, they were attributed to four possible graphitic carbon species; C–O, C=N, C=O and C–N at 284.5, 288.8 and 286.2 eV respectively. After methylene blue adsorption, a characteristic deconvoluted peak at 288.0 eV was identified and assigned to surface bound carbon(C) bound-SO_3^- (C–SO_3^-). The additional detection of sulfur peaks at ~167.5 eV, were indicative of sulfur inclusion onto the surface of ZnO@N-doped C. Whilst fluorescein also presents with carbon and oxygen atoms within its structure, the detection of sulfur and nitrogen (originating from methylene blue) in the XPS spectra lends support to identify the superior degradation of methylene blue over fluorescein (Figure 40) through non-covalent interactions (no chemical Zn shifting). The authors'[64] postulated the numerous electrostatic interactions between ZnO@N-doped C and methylene blue amino

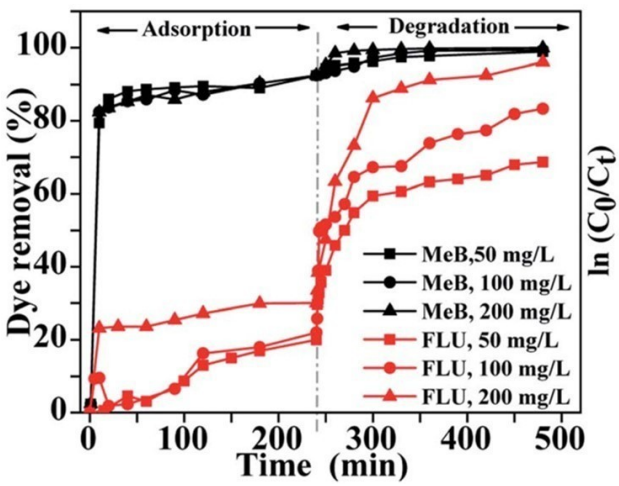

Figure 40. Photo-degradation of methylene blue and fluorescein under 450 w medium pressure mercury vapour lamp. Adapted with permission from Ref. [64] Copyright (2022) The Royal Society of Chemistry.

components (S, N, C) favoured the strong binding and hence efficient photodegradation over fluorescein (methylene blue adsorption capacity = 900 mg/g ZnO@N doped C and fluorescein adsorption capacity = 100 mg/g ZnO@N doped C) at degradation efficacies of 90% at 50 ppm using 200 mg/l ZnO@N doped C.

Continuing the study of organic dye-stuff photodegradations, Yu *et al.*[67] monitored the photo-catalytic decomposition of methyl orange, rhodamine B, and eosin B under a simulated solar spectrum after the development and application of dendritic cadmium sulfide assemblies (Figure 41).

Figure 41 monitored the photocatalytic decomposition of eosin B (99% after 80 minutes, image a), methyl orange (92% after 180 minutes, image b) and rhodamine B (>97% after 220 minutes, image c) while using dendritic cadmium sulfide under visible light irradiation. When fabricating novel photo-catalysts, researchers focus on size and shape to ensure the highest photo-catalytic response of their newly formulated semiconductors.[68] The efficiency and compatibility of the cadmium sulfide towards the photo-degradation of three organic dyestuffs were subsequently explored using SEM analyses to probe the morphology of the cadmium sulfide surface (Figure 42).

Figure 42 demonstrates the potential of HRTEM to differentiate the various crystallographic planes of a solid-state material in heterogeneous photocatalysis. Figure 42 (image c*) and (image d*) represents the circled regions in Figure 42 (image b*) for the cadmium sulfide trunk and dendrite, respectively. The recorded lattice values of 0.39 and 0.33 nm correlate to the crystal plane data and furthermore characterise the spacing between two [1010] and two [0001] crystal planes, respectively. High-resolution transmission electron microscopy has been well reported in the literature as a reliable technique to aid in identifying the crystallographic phases of metal oxides through the identification of unique lattice d-spacings for each polymorph, respectively.[69–73] Metal chalcogens have the superior property of being insoluble in most organic solvents when driving catalytic reactions are concerned. They are also favourably simple to utilise in preparatory methods when anchoring co-catalyst (organic) molecules to the functional groups on the metal oxide's surface (–OH, –COOH, –CHO).

Valence and conduction band engineering on TiO_2 has received further study from Taghavi and co. workers[74] using an approach of combining a Lewis acidic deep eutectic solvent (DES, urea: $ZnCl_2$) through toluene diisocyanate (TDI, as an organic linker) onto TiO_2 (n-TiO_2–P25@TDI@DES, Figure 43). TiO_2 was utilised as a catalytic support, whereafter the deep eutectic solvent was applied to oxidise numerous benzylic alcohols in the presence of sodium nitrate as oxidant.

The two-step approach (Figure 43) was developed to bi-link the eutectic solvent (urea: $ZnCl_2$) through the TDI linker onto TiO_2 and the promote alcohol oxidations through the available (and bound) acidic Lewis sites. Electron donating substituted benzyl alcohols (R=OCH_3, CH_3) were oxidised at 80–83% yields after 11–13 hours, meanwhile electron withdrawing substituted benzyl alcohols (R=Br, NO_2, Cl) were oxidised at 65–78% after 17–22 hours.

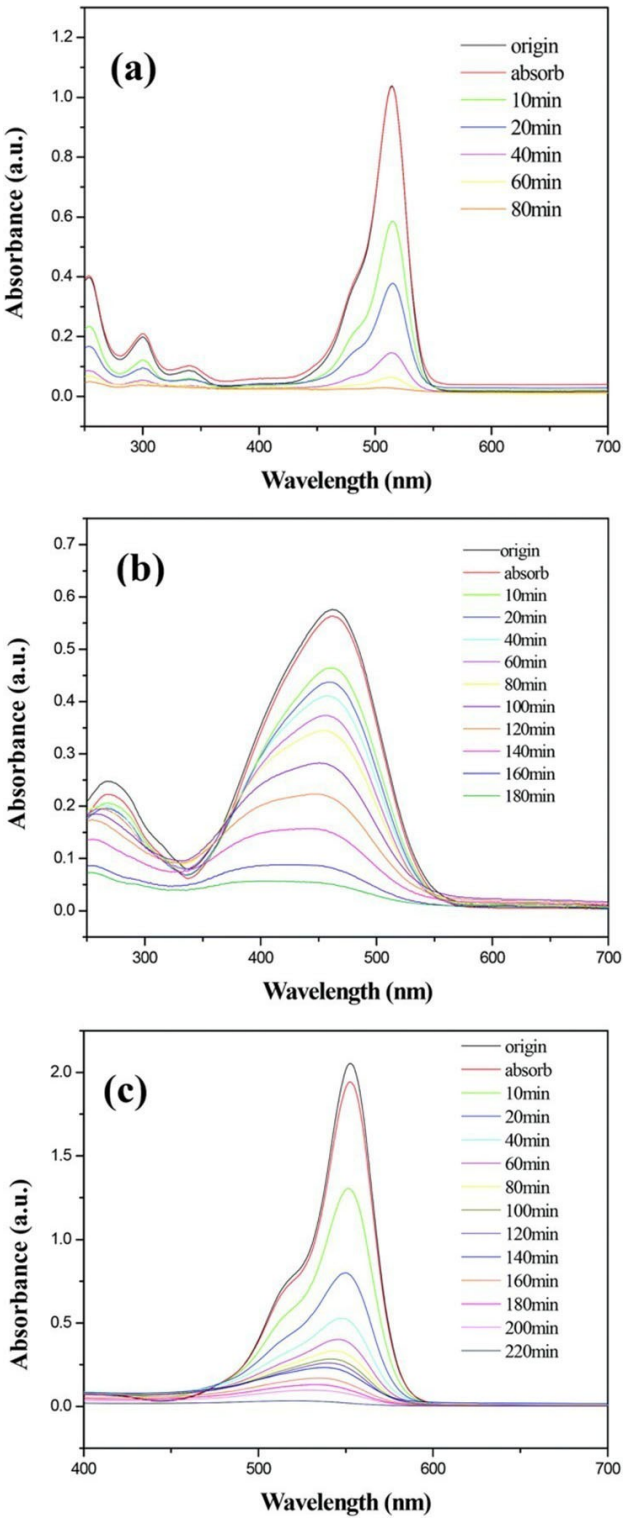

Figure 41. The photo-degradation timelines of (image a) eosin B, (image b) methyl orange and (image c) rhodamine B in the presence of dendritic cadmium sulfide assemblies under visible light irradiation. Adapted with permission from Ref. [67] Copyright (2014) The Royal Society of Chemistry.

Potentially under-utilised, yet extremely powerful is the application of Fourier transform infrared spectroscopy. In the authors' study, Taghavi *et al.*[74] monitored bound and un-bound

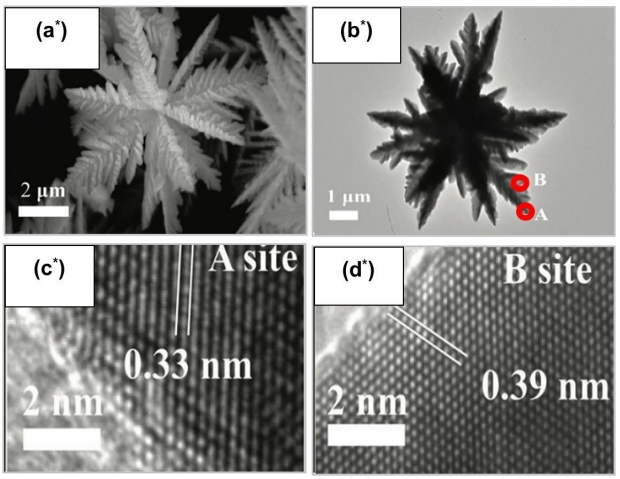

Figure 42. Dendritic structure of CdS (SEM images a*, b*). HRTEM micrographs with lattice *d*-spacings (images c* and d*) were taken at sites A and B on image b*. Adapted with permission from Ref. [67] Copyright (2014) The Royal Society of Chemistry.

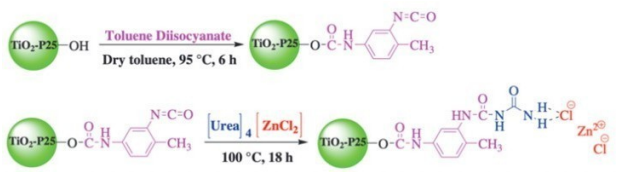

Figure 43. Synthetic approach towards n-TiO_2-P25@TDI@DES from TiO_2–P25, TDI and DES. Adapted with permission from Ref. [74] Copyright (2021) John Wiley and Sons.

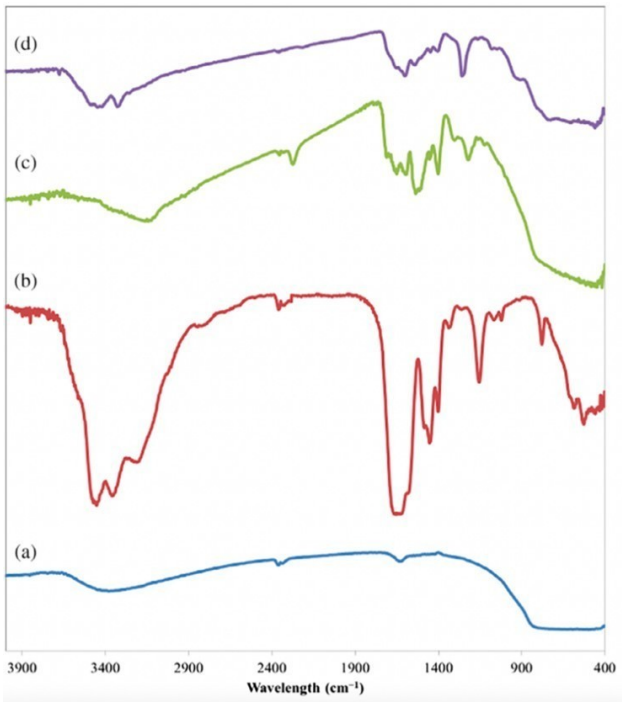

Figure 44. FT-IR spectra of pure and doped TiO_2; (a) n-TiO_2–P25, (b) DES, (c) n-TiO_2–P25@TDI and (d) n-TiO_2–P25@TDI@DES. Adapted with permission from Ref. [74] Copyright (2021) John Wiley and Sons.

TiO_2 using FT-IR and the functionalisation stages throughout attaching TDI and DES onto the metal oxide's surface (Figure 44).

TiO_2 has known weakly- and strongly- bound surface hydroxy groups that desorb at temperatures of 120–300 and 300–600 °C, respectively.[74,75] Having knowledge of this information can greatly assist with the preparation of binding organic linkers to TiO_2 through these intrinsic hydroxy groups. Taghavi *et al.*[74] observed 1623 and 3355 cm^{-1} stretching frequencies assigned to surface bound –OH groups on TiO_2. This information confirmed the viability of anchoring the first scaffold (TDI) to TiO_2, and subsequently the covalently grafted urea:$ZnCl_2$ deep eutectic solvent, with indicative 1664, 1332, 3360, and 3473 cm^{-1} vibrational peaks assigned to C=O, C–N and N–H of urea.

The technique of material coupling for the purpose of developing efficient solar photochemical compounds has the potential of being highly efficient, and significant for advances in photocatalysis. More importantly, developing strategies that reduce the fundamental question that all photocatalytic chemists and materials scientist face – limiting exciton recombination is critical for enhancing the field of semiconductor mediated photocatalysis. del-Caastillo *et al.*,[76] explored a contemporary approach of *photonic up-conversion*. The authors'[76] developed a core-shell semiconductor based on rare-earth (RE) doped up-conversion fluorides ($Sr_2YbF_7:Tm^{3+}@Sr_2YF_7$) that has the potential to absorb near infrared radiation (NIR) and *up-convert* it to higher-energies (lower wavelength). Thereafter can be absorbed and utilised by wide band gap semiconductor species for methylene blue degradation. del-Caastillo *et al.*,[76] applied the methodology of $Sr_2YbF_7:Tm^{3+}@Sr_2YF$ core-sell nanoparticles to absorb, isolate and transfer NIR radiation to TiO_2 in an isolated photo-reactor system, Figure 45).

A photocatalytic system utilising a core ($Sr_2YbF_7:Tm^{3+}$)-shell (Sr_2YF_7) arrangement was prepared via a high pressure/low temperature (< 250 °C) solvothermal method, using oleic acid to prevent aggregation and control morphological growth of the nanocrystals. Both $Sr_2YbF_7:Tm^{3+}$ core and $Sr_2YbF_7:Tm^{3+}@Sr_2YF_7$ core-shell depicted uniform morphological distribution of 9–10 and 11–13 nm, respectively. Meanwhile HRTEM imagery demonstrated that clear lattice fringes of 2.83 Å confirmed the (204) plane of Sr_2YbF_7 nanocrystals' tetragonal phase. Core luminescence arose from the sensitiser ytterbium (Yb^{3+}) ions that produced a strong absorption cross section at approximately 980 nm during NIR irradiation. Therefore, the up-conversion properties of the core luminescent Yb^{3+} centres were utilised as spectral converters of NIR to UV light. Meanwhile, the shell (Sr_2YF_7) was epitaxially grown on the core nanocrystals to promote surface quenching reduction (confirmation of the observed differences in the X-ray diffraction peaks' positions [Figure 46] were reportedly validation practises of the Sr_2YF_7 shell being successfully grown epitaxially around the core ($Sr_2YbF_7:Tm^{3+}$) nanocrystals.

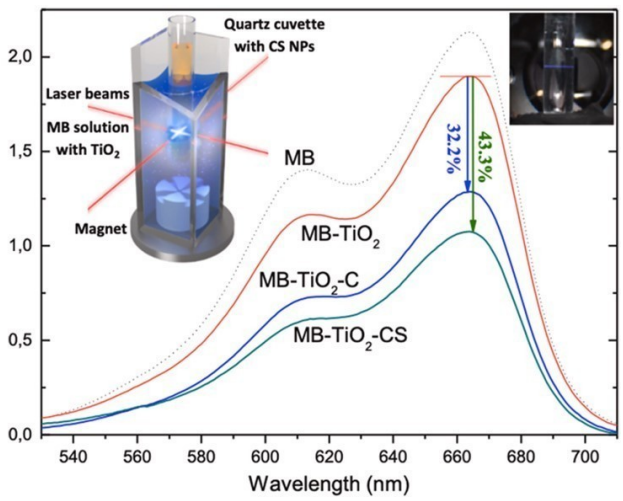

Figure 45. Methylene blue absorption studies using an isolated test tube (containing $Sr_2YbF_7:Tm^{3+}@Sr_2YF_7$ core shell nanoparticles) in a cuvette containing a mixture of titanium dioxide and 10 ppm methylene blue solution. The absorption spectra reported includes the starting adsorption-desorption (1.5-hour dark period) graph (MB-TiO_2, dotted), 300 mW (980 nm) excitation (1.5-hour period) of $Sr_2YbF_7:Tm^{3+}$ nanocrystals (MB–TiO_2–C) and $Sr_2YbF_7:Tm^{3+}@Sr_2YF_7$ core-shell nanocrystals (MB-TiO_2-CS). 3D setup represented in digital photograph insert. 32.2% and 43.3% correspond to 100 ppm methylene blue degradation using core ($Sr_2YbF_7:Tm^{3+}$) and core-shell ($Sr_2YbF_7:Tm^{3+}@Sr_2F_7$ nanocrystals respectively. Adapted with permission from Ref. [76] Copyright (2022) Elsevier.

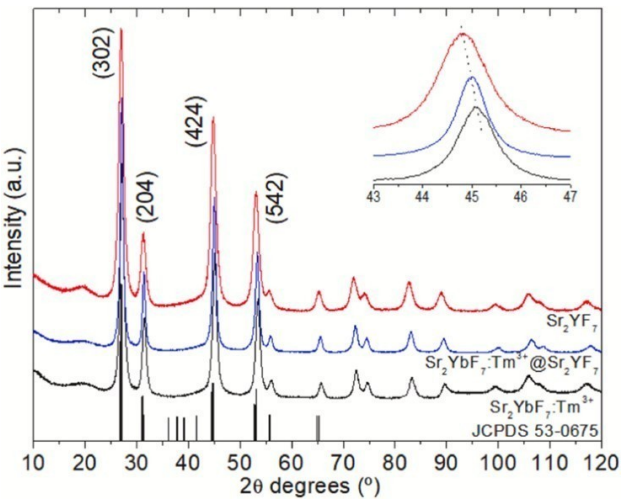

Figure 46. X-ray diffractograms of shell (Sr_2YF_7, red line), core-shell ($Sr_2YbF_7:Tm^3@Sr_2YF_7$, blue line) and shell ($Sr_2YbF_7:Tm^3$, black line) nanocrystals. Inset of the three nanocrystals with emphasis on $Sr_2YbF_7:Tm^3@Sr_2YF_7$, depicting the medial peak positioning at approximately 45°. This finding lent support for the core-shell epitaxial growth of Sr_2YF_7 on $Sr_2YbF_7:Tm^3$ core nanocrystals. Adapted with permission from Ref. [76] Copyright (2022) Elsevier.

As observed in the X-ray diffraction data, the observed intermediate shift (Figure 46, inset) for the $Sr_2YbF_7:Tm^{3+}@Sr_2YF_7$ core-shell nanocrystals were detected between those of $Sr_2YbF_7:Tm^{3+}$ and the shell nanocrystals (Sr_2YF_7), thus supporting the core-shell architecture assumption by the authors. However, the theory of the up conversion, and therefore the ability of $Sr_2YbF_7:Tm^{3+}@Sr_2YF_7$ core-shell was the fundamental nature of the photocatalytic process. Developing a plausible understanding of the photoelectronic mechanism was crucial to understanding the overall photo-physical function of $Sr_2YbF_7:Tm^{3+}@Sr_2YF_7$ core-shells (Figure 47).

The overall efficiency of $Sr_2YbF_7:Tm^{3+}@Sr_2YF_7$ core-shells to photodegrade methylene blue was reported at a modest 43.3%. During the proposed photo-degradative processes, $Sr_2YbF_7:Tm^{3+}@Sr_2YF_7$ core-shells were excited by NIR irradiation, and as observed in the inset of Figure 47, a $^2F_{7/2}$ to $^2F_{5/2}$ transition was assigned to the transition of Yb^{3+} ions. After NIR excitation of $Sr_2YbF_7:Tm^{3+}@Sr_2YF_7$ core-shells, Yb^{3+} acted as large IR collectors that facilitated photoelectronic migrations through the $^2F_{7/2}$ to $^2F_{5/2}$ transition and into the Tm^{3+} ions, of which energy transfer mechanisms have been previously discussed in the literature.[77] After Tm^{3+} received the incoming radiation, TiO_2 absorbed the up converted emission energy from Tm^3 and therefore facilitating the methylene blue degradation in-solution (Figure 45).

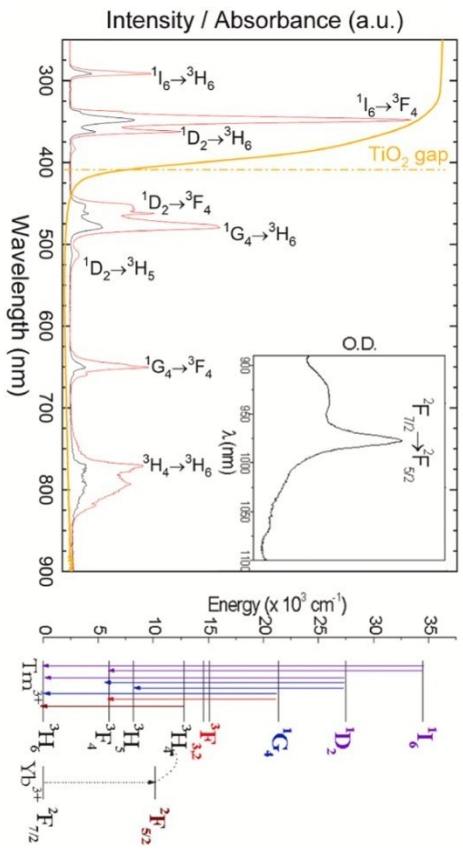

Figure 47. Up conversion emission spectra of $Sr_2YbF_7:Tm^{3+}$ (black line) and $Sr_2YbF_7:Tm^{3+}@Sr_2YF_7$ (red line). The excitation wavelength was a 300 mW, 980 nm pump source that was focussed with an objective lens. For reference, high energy bands above the band gap of TiO_2 (above 3.2 eV, 415 nm) are depicted (orange line) and the inset shows the absorbance maxima of Tb^{3+} at 980 nm, corresponding to the NIR laser excitation wavelength. Adapted with permission from Ref. [76] Copyright (2022) Elsevier.

2. Summary and Outlook

This review has made the attempt to correlate the relationship between modern instrumental techniques and 'active' photocatalytic materials to further the understanding of photophysical properties that govern the success of a photo-organic transformation using heterogeneous semiconductors. Through several case studies that utilised ZnO, CdS, WO_3, Fe_2O_3, Cu_2O, TiO_2, $CaFe_2O_4$ with doping and-or co-doping, heterojunction strategies (N, Pd, Ag, Pt, Sn, alizarin red, α-Fe_2O_3, $ZnWO_4$, SnO_2), numerous alcohol oxidations, CO_2 to CO and CH_4, CH_3CHO to CO_2 and organic dyestuff degradations (methyl orange, rhodamine B, eosin Y) have been reported. The application of various instrumental techniques, amongst which, include powder X-ray diffraction, methyl-iodide chemical ionisation mass-spectrometry, ultraviolet spectroscopy, infrared spectroscopy microscopic analyses, photoluminescence spectroscopy, electron paramagnetic spectroscopy demonstrate the value of vital solid-state information to extend the understanding of the nature and photo-physics of the above-mentioned semiconductors. Whilst this review has not explored the performance of the described metal oxide photocatalysts, significant consideration to develop critical consideration by the readership has been included to stimulate unconsidered knowledge generation and "out-of-the-box" thinking-applications of modern instrumentation.

The production capacity of photocatalytic materials is still far below an industrial value to match conventional redox agents. Extensions to future research which enhance the efficacy of semiconductor materials at greater turnover numbers in the presence of natural visible light can be envisaged. The literature is abundant with upcoming research topics; $Bi_2WO_6ZnWO_4$ with Bi^{3+} ion introduction, reducing the band gap from 4.7 to 3.5 eV for photodegrading plasmocorinth B, a designed-alternative-stacking approach of CdS loaded on hollow carbon, followed by $ZnIn_2S_4$ (C/CdS@$ZnIn_2S_4$) for photochemical control of CO_2-to-CO conversion and developing Schottky junction heterojunction photocatalysts using hydrothermal processes ($ZnIn_2S_4$/WC) for hydrogen production (up to 2400.3 μmol h^{-1} g_{cat}^{-1}).[78–80] The continual exploring of heterojunctions, Schottky Barriers and novel photocatalytic techniques will surely extend the knowledge basis tremendously.

For the evolution of photocatalysis to occur (and reach industrial scale practicality), novel methods of design, synthesis and applications of metal oxides need to originate from understanding the fundamental photo-physics. These start with enhanced instrumental investigations and unconventional adaptations.

Permissions acknowledgement

Acknowledgements

Special acknowledgement to the National Research Foundation and secondly, ESKOM TESP for their financial support of the greater research arising from the studies conducted herein.

Conflict of Interest

The authors declare no conflict of interest.

Keywords: photocatalysts · instrumental insight · heterogeneous catalysis · spectroscopy and microscopy · band gap engineering

[1] S. Trépout, *Materials* **2019**, *12*, 2281.
[2] a) L. Liao, D. Ditz, F. Zeng, M. Alves Favaro, A. Iemhoff, K. Gupta, H. Hartmann, C. Szczuka, P. Jakes, P. J. C. Hausoul, J. Artz, R. Palkovits, *ChemistrySelect* **2020**, *5*, 14438–14446; b) C. M. T. Su, L. Chen, B. Chu, X. Luo, H. Ji, J. Chen, Z. Qin, *Adv. Sci.* **2022**, *9*, 2103715; c) W. Li, R. Liang, N. Y. Zhou, Z. Pan, *ACS Omega* **2020**, *5*, 10042–10051; d) M. Mohammadi, H. Hadadzadeh, M. Kaikhosravi, H. Farrokhpour, J. Shakeri, *J. Mol. Catal.* **2020**, *490*, 110927; e) J. Zou, Z. Wang, W. Guo, B. Guo, Y. Yu, L. Wu, *Appl. Catal. B* **2019**, *260*, 118185; f) H. Sakamoto, J. Imai, Y. Shiraishi, S. Tanaka, S. Ichikawa, T. Hirai, *ACS Catal.* **2017**, *7*, 5194–5201; g) S. Balachandran, S. G. Praveen, R. Velmurugan, M. Swaminathan, *RSC Adv.* **2014**, *4*, 4353–4362; h) X.-F. Gao, W.-T. Sun, Z.-D. Hu, G. Ai, Y.-L. Zhang, S. Feng, F. Li, L.-M. Peng, *J. Phys. Chem. C* **2009**, *113*, 20481–20485; i) S. Liu, N. Zhang, Z.-R. Tang, Y.-J. Xu, *ACS Appl. Mater. Interfaces* **2012**, *4*, 6378–6385; j) A. Hamrouni, N. Moussa, A. Di Paola, L. Palmisano, A. Houas, F. Parrino, *J. Photochem. Photobiol. A* **2015**, *309*, 47–54; k) Z. Yang, X. Xu, X. Liang, C. Lei, Y. Cui, W. Wu, Y. Yang, Z. Zhang, Z. Lei, *Appl. Catal. B* **2017**, *205*, 42–54; l) J.-C. Wang, L. Zhang, W.-X. Fang, J. Ren, Y.-Y. Li, H.-C. Yao, J.-S. Wang, Z.-J. Li, *ACS Appl. Mater. Interfaces* **2015**, *7*, 8631–8639; m) Y. Zhen, C. Yang, H. Shen, W. Xue, C. Gu, J. Feng, Y. Zhang, F. Fu, Y. Liang, *Phys. Chem. Chem. Phys.* **2020**, *22*, 26278–26288; n) C. Cheng, J. Zhang, R. Zeng, F. Xing, C. Huang, *Appl. Catal. B* **2022**, *310*, 121321.
[3] F. Fischer, *Renewable Sustainable Energy Rev.* **2018**, *90*, 16–27.
[4] M. Nishikawa, S. Yuto, T. Nakajima, T. Tsuchiya, N. Saito, *Catal. Lett.* **2017**, *147*, 292–300.
[5] B. Trujillo-Navarrete, M. del Pilar Haro-Vázquez, R. M. Félix-Navarro, F. Paraguay-Delgado, H. Alvarez-Huerta, S. Pérez-Sicairos, E. A. Reynoso-Soto, *J. Rare Earth* **2017**, *35*, 259–270.
[6] J. Low, J. Yu, M. Jaroniec, S. Wageh, A. A. Al-Ghamdi, *Adv. Mater.* **2017**, *29*, 1601694.
[7] I. Aslam, C. Cao, M. Tanveer, M. H. Farooq, W. S. Khan, M. Tahir, F. Idrees, S. Khalid, *RSC Adv.* **2015**, *5*, 6019–6026.
[8] C. Shifu, J. Lei, T. Wenming, F. Xianliang, *Dalton Trans.* **2013**, *42*, 10759–10768.
[9] Y. Zang, L. Li, Y. Zuo, H. Lin, G. Li, X. Guan, *RSC Adv.* **2013**, *3*, 13646–13650.
[10] S. Sze, K. K. Ng, *Physics and Properties of Semiconductors – A Review,* 3 ed., John Wiley & Sons, INC, New Jersey, **2006**, p. 58.
[11] J. Low, C. Jiang, B. Cheng, S. Wageh, A. A. Al-Ghamdi, J. Yu, *Small Methods* **2017**, *1*, 1700080.
[12] Z. Yang, X. Xu, X. Liang, C. Lei, Y. Wei, P. He, B. Lv, H. Ma, Z. Lei, *Appl. Catal. B* **2016**, *198*, 112–123.
[13] R. Fagan, D. E. McCormack, S. J. Hinder, S. C. Pillai, *Materials* **2016**, *9*, 286.
[14] W. Maziarz, A. Kusior, A. Trenczek-Zajac, *Beilstein J. Nanotechnol.* **2016**, *7*, 1718–1726.
[15] L. Yang, Z. Liu, *Energy Convers. Manage.* **2007**, *48*, 882–889.
[16] S. Anandan, M. Miyauchi, *Chem. Commun.* **2012**, *48*, 4323–4325.
[17] Q. Xu, L. Zhang, B. Cheng, J. Fan, J. Yu, *Chem* **2020**, *6*, 1543–1559.
[18] J. Yu, S. Wang, J. Low, W. Xiao, *Phys. Chem. Chem. Phys.* **2013**, *15*, 16883–16890.
[19] Y. Liu, G. Ji, M. A. Dastageer, L. Zhu, J. Wang, B. Zhang, X. Chang, M. A. Gondal, *RSC Adv.* **2014**, *4*, 56961–56969.

[20] L. Nie, Y. Zheng, J. Yu, *Dalton Trans.* **2014**, *43*, 12935–12942.
[21] Y. Zhong, J. Yuan, J. Wen, X. Li, Y. Xu, W. Liu, S. Zhang, Y. Fang, *Dalton Trans.* **2015**, *44*, 18260–18269.
[22] Y. Su, P. Chen, F. Wang, Q. Zhang, T. Chen, Y. Wang, K. Yao, W. Lv, G. Liu, *RSC Adv.* **2017**, *7*, 34096–34103.
[23] H. Wang, H. Ye, B. Zhang, F. Zhao, B. Zeng, *J. Mater. Chem. A* **2017**, *5*, 10599–10608.
[24] J. Fu, S. Cao, J. Yu, *J. Materiomics.* **2015**, *1*, 124–133.
[25] H. Li, W. Tu, Y. Zhou, Z. Zou, *Adv. Sci.* **2016**, *3*, 1500389.
[26] M. Miyauchi, Y. Nukui, D. Atarashi, E. Sakai, *ACS Appl. Mater. Interfaces* **2013**, *5*, 9770–9776.
[27] R. Mishra, S. Bera, R. Chatterjee, S. Banerjee, S. Bhattacharya, A. Biswas, S. Mallick, S. Roy, *J. Apsadv.* **2022**, *9*, 100241.
[28] J. Fu, Q. Xu, J. Low, C. Jiang, J. Yu, *Appl. Catal. B* **2019**, *243*, 556–565.
[29] W. Bootluck, T. Chittrakarn, K. Techato, P. Jutaporn, W. Khongnakorn, *Catal. Lett.* **2022**, *152*, 2590–2606.
[30] L. Zhang, J. Zhang, H. Yu, J. Yu, *Adv. Mater.* **2022**, *34*, 2107668.
[31] H. Rongan, L. Haijuan, L. Huimin, X. Difa, Z. Liuyang, *J. Mater. Sci. Technol.* **2020**, *52*, 145–151.
[32] C. Cheng, B. He, J. Fan, B. Cheng, S. Cao, J. Yu, *Adv. Mater.* **2021**, *33*, 2100317.
[33] H. Cheng, K. Fuku, Y. Kuwahara, K. Mori, H. Yamashita, *J. Mater. Chem. A* **2015**, *3*, 5244–5258.
[34] A. G. Milekhin, L. L. Sveshnikova, T. A. Duda, N. A. Yeryukov, E. E. Rodyakina, A. K. Gutakovskii, S. A. Batsanov, A. V. Latyshev, D. R. T. Zahn, *Phys. E* **2016**, *75*, 210–222.
[35] L. Gomathi Devi, R. Kavitha, *Appl. Surf. Sci.* **2016**, *360*, 601–622.
[36] C. Han, Q. Quan, H. M. Chen, Y. Sun, Y.-J. Xu, *Small* **2017**, *13*, 1602947.
[37] J. J. Mock, M. Barbic, D. R. Smith, D. A. Schultz, S. Schultz, *J. Chem. Phys.* **2002**, *116*, 6755–6759.
[38] T. Atay, J.-H. Song, A. V. Nurmikko, *Nano Lett.* **2004**, *4*, 1627–1631.
[39] K. Kolwas, A. Derkachova, M. Shopa, *J. Quant. Spectrosc. Radiat. Transfer* **2009**, *110*, 1490–1501.
[40] W. Hou, S. B. Cronin, *Adv. Funct. Mater.* **2013**, *23*, 1612–1619.
[41] K.-H. Kim, A. Husakou, J. Herrmann, *Opt. Express* **2010**, *18*, 7488–7496.
[42] X. Ma, X. Wu, Y. Wang, Y. Dai, *Phys. Chem. Chem. Phys.* **2017**, *19*, 18750–18756.
[43] A. A. Ashkarran, A. Bayat, *Int. Nano Lett.* **2013**, *3*, 50.
[44] J. P. A. de Jesus, A. C. L. Santos, F. M. Pinto, C. A. Taft, F. A. La Porta, *J. Mater. Sci.* **2021**, *56*, 4552–4568.
[45] L. Wang, S. Chen, W. Li, K. Wang, Z. Lou, G. Shen, *Adv. Mater.* **2019**, *31*, 1804583.
[46] M. Li, Z. Zhang, X. Ge, Z. Wei, Y. Yao, H. Chen, C. Wang, F. Du, G. Chen, *Chem. Eng. J.* **2018**, *331*, 203–210.
[47] X. Cheng, X. Yu, Z. Xing, J. Wan, *Energy Procedia* **2012**, *16*, 598–605.
[48] S. A. Ansari, M. M. Khan, M. O. Ansari, M. H. Cho, *New J. Chem.* **2016**, *40*, 3000–3009.
[49] X. Chen, Z. Zheng, X. Ke, E. Jaatinen, T. Xie, D. Wang, C. Guo, J. Zhao, H. Zhu, *Green Chem.* **2010**, *12*, 414–419.
[50] Y. Shiraishi, H. Sakamoto, Y. Sugano, S. Ichikawa, T. Hirai, *ACS Nano* **2013**, *7*, 9287–9297.
[51] M. Cherevatskaya, B. König, *Russ. Chem. Rev.* **2014**, *83*, 183–195.
[52] J. Bardeen, *Phys. Rev.* **1947**, *71*, 717–727.
[53] V. Heine, *Phys. Rev.* **1965**, *138*, A1689–A1696.
[54] R. T. Tung, *Appl. Phys. Rev.* **2014**, *1*, 011304.
[55] G.-S. Kim, S.-W. Kim, S.-H. Kim, J. Park, Y. Seo, B. J. Cho, C. Shin, J. H. Shim, H.-Y. Yu, *ACS Appl. Mater. Interfaces* **2016**, *8*, 35419–35425.
[56] J. Zhang, C. Cheng, F. Xing, C. Chen, C. Huang, *Chem. Eng. J.* **2021**, *414*, 129157.
[57] K. Zhang, L. Guo, *Catal. Sci. Technol.* **2013**, *3*, 1672–1690.
[58] L. Huang, B. Li, B. Su, Z. Xiong, C. Zhang, Y. Hou, Z. Ding, S. Wang, *J. Mater. Chem. A* **2020**, *8*, 7177–7183.
[59] A. T. Kuvarega, R. W. M. Krause, B. B. Mamba, *J. Phys. Chem. C* **2011**, *115*, 22110–22120.
[60] H. Wang, D. Yong, S. Chen, S. Jiang, X. Zhang, W. Shao, Q. Zhang, W. Yan, B. Pan, Y. Xie, *J. Am. Chem. Soc.* **2018**, *140*, 1760–1766.
[61] G. T. Tyuliev, K. L. Kostov, *Phys. Rev. B* **1999**, *60*, 2900–2907.
[62] H. Qian, G. Yu, Q. Hou, Y. Nie, C. Bai, X. Bai, H. Wang, M. Ju, *Appl. Catal. B* **2021**, *291*, 120064.
[63] A. Bavykina, N. Kolobov, I. S. Khan, J. A. Bau, A. Ramirez, J. Gascon, *Chem. Rev.* **2020**, *120*, 8468–8535.
[64] A. I. A. Soliman, A.-M. A. Abdel-Wahab, H. N. Abdelhamid, *RSC Adv.* **2022**, *12*, 7075–7084.
[65] H. N. Abdelhamid, X. Zou, *Green Chem.* **2018**, *20*, 1074–1084.
[66] R. Grau-Crespo, A. Aziz, A. Collins, R. Crespo, N. Hernández, L. Rodriguez-Albelo, A. R. Ruiz-Salvador, S. Calero, S. Hamad Gomez, *Angew. Chem. Int. Ed.* **2016**, *55*, 16012–16016; *Angew. Chem.* **2016**, *128*, 16246–16250.
[67] Z. Yu, F. Qu, X. Wu, *Dalton Trans.* **2014**, *43*, 4847–4853.
[68] S. Yurdakal, V. Augugliaro, *RSC Adv.* **2012**, *2*, 8375–8380.
[69] L. Zhu, Q. Lu, L. Lv, Y. Wang, Y. Hu, Z. Deng, Z. Lou, Y. Hou, F. Teng, *RSC Adv.* **2017**, *7*, 20084–20092.
[70] Y. Liao, W. Que, Q. Jia, Y. He, J. Zhang, P. Zhong, *J. Mater. Chem.* **2012**, *22*, 7937–7944.
[71] D. Reyes-Coronado, G. Rodríguez-Gattorno, M. E. Espinosa-Pesqueira, C. Cab, R. de Coss, G. Oskam, *Nanotechnology* **2008**, *19*, 145605.
[72] P. Bindu, S. Thomas, *J. Theor. Appl. Phys* **2014**, *8*, 123–134.
[73] S. Verma, S. L. Jain, *Inorg. Chem. Front.* **2014**, *1*, 534–539.
[74] S. Taghavi, A. Amoozadeh, F. Nemati, *J. Chem. Technol. Biotechnol.* **2021**, *96*, 384–393.
[75] C.-Y. Wu, K.-J. Tu, J.-P. Deng, Y.-S. Lo, C.-H. Wu, *Materials* **2017**, *10*, 566.
[76] J. del-Castillo, J. Méndez-Ramos, P. Acosta-Mora, A. C. Yanes, *J. Lumin.* **2022**, *241*, 118490.
[77] J. del-Castillo, A. C. Yanes, *Phys. Chem. Chem. Phys.* **2018**, *20*, 20910–20918.
[78] P. Kumar, S. Verma, N. Č. Korošin, B. Žener, U. L. Štangar, *Catal. Today* **2021**, *397–399*, 278–285.
[79] X. Zhang, P. Wang, X. Lv, X. Niu, X. Lin, S. Zhong, D. Wang, H. Lin, J. Chen, S. Bai, *ACS Catal.* **2022**, *12*, 2569–2580.
[80] X. Ma, W. Li, C. Ren, H. Li, X. Li, M. Dong, Y. Gao, T. Wang, H. Zhou, Y. Li, *J. Alloys Compd.* **2022**, *901*, 163709.

Manuscript received: April 11, 2022
Revised manuscript received: July 25, 2022
Accepted manuscript online: August 14, 2022
Version of record online: September 1, 2022